

Radar Observations of Asteroid 2063 Bacchus

LANCE A. M. BENNER

Jet Propulsion Laboratory, California Institute of Technology, Pasadena, CA 91109-8099
E-mail: lance@think.Jpl.Nasa.Gov

R. SCOTT HUDSON

School of Electrical Engineering and Computer Science
Washington State University, Pullman, WA 99164-2752

STEVEN J. OSTRO, KEITH D. ROSEMA, JON D. GIORGINI, DONALD K. YEOMANS,
RAYMOND F. JURGENS, DAVID L. MITCHELL,[†] RON WINKLER, RANDY ROSE,
MARTIN A. SLADE, AND MICHAEL L. THOMAS

Jet Propulsion Laboratory, California Institute of Technology, Pasadena, CA 91109-8099

AND

PETR PRAVEC

Astronomical Institute, Academy of Sciences of the Czech Republic
CZ-25165 Ondrejov, Czech Republic

Author	AC	voice	fax	JPL mailstop	E-mail
Benner	818	354-7412	354-9476	300-233	lance@think.jpl.nasa.gov
Hudson	509	335-0922	335-3818		hudson@eecs.wsu.edu
Ostro	818	354-3173	354-9476	300-233	ostro@echo.jpl.nasa.gov
Rosema	818	393-2629	354-9476	300-233	rosema@think.jpl.nasa.gov
Giorgini	818	393-3107	393-1159	301-150	jdj@tycho.jpl.nasa.gov
Yeomans	818	354-2127	393-1159	301-150	Donald.K.Yeomans@jpl.nasa.gov
Jurgens	818	354-4974	354-6825	238-420	jurgens@bvd.jpl.nasa.gov
Mitchell	818	354-9474	354-9476	300-233	mitchell@think.jpl.nasa.gov
Winkler	619	255-8259	255-8515	DSCC-61	winkler@intruder.gdscc.nasa.gov
Rose	619	255-8259	255-8515	DSCC-61	rose@intruder.gdscc.nasa.gov
Slade	818	354-2765	354-6825	238-420	marty@shannon.jpl.nasa.gov
Thomas	818	393-3085	354-9476	300-233	wart@echo.jpl.nasa.gov
Pravec		+00420-2-881611			ppravec@asu.cas.cz

40 manuscript pages (or 29 excluding tables and figure captions)

13 figures, 7 tables

Keywords: asteroids, radar, Bacchus

[†]Present address: Space Sciences Laboratory, University of California, Berkeley, CA 94720

Proposed running head: Radar observations of Bacchus

Correspondence address:

Dr. Lance A. M. Benner

Mail Stop 300-233

Jet Propulsion Laboratory

California Institute of Technology

4800 Oak Grove Drive

Pasadena, CA 91109-8099

E-mail: lance@think.jpl.nasa.gov

ABSTRACT

asteroid

We report Doppler-only (cw) and delay-Doppler radar observations of **Bacchus** obtained at Goldstone at a transmitter frequency of 8510 MHz (3.5 cm) on 1996 March 22, 24, and 29. Weighted, optimally filtered sums of cw and delay-Doppler echoes achieve signal-to-noise ratios of ~ 80 and ~ 25 , respectively, and cover about 180° of rotation phase (period = 14.90 h; Pravec *et al.* 1998). Our cw observations place up to four 2-Hz-resolution cells on Bacchus at echo powers greater than two standard deviations of the noise. Delay-Doppler observations typically place about ten $0.5\text{-}\mu\text{s}$ (75-m) \times 1-Hz cells on Bacchus above the same threshold. A weighted sum of all cw spectra gives an OC radar cross section of $0.12^{+0.06}_{-0.02} \text{ km}^2$ and a circular polarization ratio of 0.21 ± 0.01 . The dispersion of the echoes in time delay indicates a lower bound on Bacchus' maximum pole-on breadth of 0.6 km that is consistent with Bacchus' echo bandwidth (6 ± 2 Hz) and rotation period. Echo spectra on March 22 and delay-Doppler images on all three days show a central deficit of echo power that provides strong evidence for a bifurcation in the shape. Inversion of delay-Doppler images, cw spectra, and optical lightcurves obtained at Ondrejov Observatory yields single-lobe and two-lobe models that define lower and upper bounds on the degree of bifurcation. Both shape models have a prominent central concavity, modestly asymmetric shapes, and similar physical dimensions, spin vectors, and radar and optical geometric albedos. We adopt the more conservative single-lobe shape model as our working model and explore its implications. It has a radar-derived sidereal rotation period $P_{\text{sid}} = 15.0 \pm 0.2$ h and a north pole within a few tens of degrees of ecliptic longitude $\lambda = 24^\circ$ and ecliptic latitude $\beta = -26^\circ$; retrograde rotation is likely. It has dimensions of $1.11 \times 0.53 \times 0.50$ km, an effective diameter (the diameter of a sphere with the same volume as the model) $D_{\text{eff}} = 0.63^{+0.13}_{-0.06}$ km, and radar and optical geometric albedos $\hat{\sigma} = 0.33^{+0.25}_{-0.11}$ and $p_v = 0.56^{+0.12}_{-0.18}$, respectively, that are larger than most estimated for any aster-

oid. Bacchus' low circular polarization ratio and the high radar albedo are consistent with nearly regolith-free ordinary chondrite and basaltic achondrite compositions, but its high optical geometric albedo seems inconsistent with an ordinary chondrite composition and may favor a V-class composition. Bacchus has less structural complexity at centimeter-to-decimeter spatial scales and its near-surface is more dense (either more metal, lower porosity, or both) than the average radar-detected near-Earth asteroid.

1. INTRODUCTION

Near-Earth asteroid 2063 Bacchus (1977 HB) approached within 0.0678 AU of Earth on 1996 March 31, its closest terrestrial encounter until 2271. Bacchus was discovered by C. Kowal (1977) at Palomar on 1977 April 24, but prior to the 1996 encounter, the asteroid's rotation period, pole direction, geometric albedo, visible and near-infrared spectrum, taxonomic class, and shape were unknown. Photometry of Bacchus by Pravec *et al.* (1998) in March-April, 1996 yielded a synodic rotation period of 14.904 ± 0.003 hours and a maximum lightcurve amplitude of ~ 0.4 magnitudes. Binzel *et al.* (1996) and Hicks *et al.* (1998) found that Bacchus' visible-near infrared spectrum resembles those of the "average" H-chondrites and Q-class near-Earth asteroid (NEA) 1862 Apollo, but Hicks *et al.* (1998) note that the spectrum is also similar to that of V-class asteroid 4 Vesta. In contrast, Lazzarin *et al.* (1997) obtained an optical spectrum that they interpreted as indicative of the C-class. Table I summarizes the optically-derived properties of Bacchus.

Here we present radar observations of Bacchus conducted at Goldstone in March 1996. Optimally filtered, weighted sums of echo power spectra and delay-Doppler images achieve signal-to-noise ratios (SNRs) of ~ 80 and ~ 25 , respectively, that provide unique constraints on Bacchus' physical properties. Our best delay-Doppler images place about 10 pixels on Bacchus, provide compelling evidence for a bifurcated shape. Bacchus is an unusually reflective object at radar and optical wavelengths.

2. OBSERVATIONS

Our observation and reduction techniques are similar to those described by Mitchell *et al.* (1995) and Ostro *et al.* (1992, 1996). Each observing cycle (run) consisted of transmission of a circularly polarized wave for close to the expected round-trip light travel time to the target, followed by reception of echoes for a comparable duration. In Doppler-only or continuous wave (cw) observations, echoes were received simultaneously in the opposite (OC) and same (SC) senses of circular polarization as the transmission. In delay-Doppler observations, we transmitted a continuous binary phase-coded waveform and received OC echoes.

Our reduction of raw data included background removal, calibration, and the formation of sums of spectra and images. In our images, echo power in units of standard deviations of the noise is plotted versus Doppler frequency and time delay relative to the delay/Doppler location of the target's estimated center of mass (COM). Echo power is given by

$P_R = P_T G_T G_R \lambda^2 \sigma / (4\pi)^3 R^4$, where P_T is the transmitted power, G_T and G_R are the antenna's gain during transmission and reception, λ is the wavelength (3.52 cm at the Goldstone transmitter frequency of 8510 MHz), and R is the target's distance. The radar cross section σ , which is 4π times the backscattered power per steradian per unit flux incident at the asteroid, is estimated by integrating Doppler-only echo power spectra. Uncertainties in σ are dominated by systematic pointing and calibration errors that are typically between 20% and 50%.

The circular polarization ratio $\mu_C = \sigma_{SC}/\sigma_{OC}$ is a gauge of near-surface roughness at spatial scales within about an order of magnitude of the radar wavelength (Ostro 1993). For μ_C , systematic effects cancel and most remaining statistical errors propagate from receiver noise according to Fieller's theorem (Kendall and Stuart 1979, pp. 136-138; Ostro *et al.* 1992). Another

useful intrinsic property is the OC radar albedo

$$\hat{\sigma}_{oc} = \sigma_{oc}/A = 4\sigma_{oc}/\pi D_{area}^2 \quad (1)$$

where A is the target's projected area and the areal diameter D_{area} is the diameter of a sphere with the same projected area as the target.

For objects with low μ_c , $\hat{\sigma}_{oc}$ can be related to the Fresnel reflection coefficient at normal incidence R by

$$\hat{\sigma}_{oc} = gR, \quad (2)$$

where the gain factor g depends on the target's orientation, shape, the distribution of surface slopes, and the wavelength-scale roughness. For a sphere with $\mu_c \sim 0$, g is close to unity, although for irregularly shaped asteroids g may vary strongly with orientation. For dry powdered mixtures of meteoritic materials with particle sizes less than $\sim \lambda/100$, R is a nearly linear function of density, which in turn is a function of porosity and composition. Garvin *et al.* (1985) determined an empirical relation between surface bulk density d and R that is applicable for porosities greater than $\sim 20\%$:

$$d(R) = 3.2 \ln \left[\frac{1 + \sqrt{R}}{1 - \sqrt{R}} \right]. \quad (3)$$

Echo power spectra represent one-dimensional images that can be thought of as brightness scans through a slit parallel to the target's apparent spin vector. The echo's instantaneous bandwidth B is

$$B = 4\pi D(\phi) \cos \delta / (\lambda P) \quad (4)$$

where D is the breadth of the plane-of-sky projection of the pole-on silhouette at rotation phase ϕ , P is the apparent rotation period, λ is the radar wavelength, and δ is the angle between the radar line-of-sight and the object's apparent equator. If P is known, then measuring B and setting

$\cos \delta = 1$ places a lower bound on the asteroid's maximum pole-on breadth D_{\max} . Expressing B in Hz, D in kilometers, and P in hours gives $B = 99.7 D(\text{km}) \cos \delta / P(\text{hrs})$ at $\lambda = 3.52$ cm.

Our ability to discern the echo's bandwidth depends on the signal-to-noise ratio, the target's shape, the radar scattering law, and the frequency resolution. Using our previous experience with modeling asteroid echoes as a guide, we adopt an estimator that measures spectral bandwidths using the points above and below the estimated COM frequency where the echo power exceeds two standard deviations (Benner *et al.* 1997).

Delay-Doppler images resolve the target into cells defined by planes of constant time delay that are orthogonal to the radar line of sight and by planes of constant Doppler frequency that are parallel to the radar line of sight and the target's apparent spin vector. Points on the surface from hemispheres north and south of the target's apparent equator can return echoes at the same time delay and Doppler frequency; thus, each rectangular cell may represent a two- or even several-to-one mapping of echo power from the target's three-dimensional surface onto the two-dimensional delay-Doppler array. This north-south ambiguity complicates the interpretation of delay-Doppler images.

Modeling of an image sequence that provides good rotation phase coverage at subradar latitudes off the equator is usually required to resolve the north-south ambiguity (Hudson 1993), a technique that provided powerful constraints on the three-dimensional shapes of NEAs 4769 Castalia (Hudson and Ostro 1994) and 4179 Toutatis (Hudson and Ostro 1995). Although the SNRs and rotation phase coverage of the Bacchus images are much lower than those of Toutatis or Castalia, modeling still provides useful constraints on Bacchus' shape.

Overview of the experiment

We observed Bacchus on 1996 March 22, 24, and 29 as it was approaching Earth. Key observational parameters are summarized in Table II. The available observing tracks and Bacchus' rotation period (unknown at the time of the observations) yielded slightly more than 180° of rotation phase coverage (Fig. 1).

The imaging observations used a 127-element binary phase-coded waveform with a time resolution (or "baud") as coarse as $11\ \mu\text{s}$ (where $1\ \mu\text{s}$ equals 150 m of range resolution) and as fine as $0.25\ \mu\text{s}$ (Table II). The full delay-Doppler arrays consist of 64 Doppler cells x 127 range cells, except for fourteen $0.25\ \mu\text{s}$ images, which used a 128×127 array. All images presented here are vignettted from the full delay-Doppler arrays.

The Bacchus echoes were expected to be strong enough for delay-Doppler imaging on each day of the experiment. Our objectives on the first day were to obtain cw echoes, assess the echo strengths, and estimate the Doppler correction to the ephemeris; estimate delay corrections to the prediction; update the ephemeris; and then proceed to high-resolution imaging (Fig. 1, Table II). We attempted our highest-resolution imaging with a $0.25\ \mu\text{s} \times 0.5\ \text{Hz}$ setup on March 24 but found that those echoes were too weak, so we switched to a $0.5\ \mu\text{s} \times 1\ \text{Hz}$ setup. We concluded March 24 with ten $7\ \mu\text{s} \times 5.9\ \text{Hz}$ runs to update the range. After the track on March 24, one of Goldstone's two X-band klystrons failed, reducing available transmitter power on March 29 to $\sim 250\ \text{kW}$. However, Bacchus' smaller distance on that day offset the power reduction and resulted in SNRs that were comparable to those obtained on March 24.

Table III lists the radar astrometry, which is also available on the Internet at the JPL Solar System Dynamics homepage at: http://ssd.jpl.nasa.gov/radar_data.html (Chamberlin *et al.* 1997). Astrometry obtained on March 22 was entered into the JPL On Site Orbital Determination

(OSOD) program and was used to generate a new ephemeris (solution 6) which we used on the final two days. After the experiment concluded, we generated orbital solution 11 using astrometry obtained on March 24 and 29 and optical astrometry obtained through the end of 1997 (Table IV).

We estimated COM frequencies iteratively, starting with preliminary estimates that used the central frequency from weighted sums of echo power spectra obtained on each day, then by adopting the apparent midpoints of high-resolution images obtained on each day, and ultimately from the shape modeling. Confidence in our COM frequency estimates is bolstered by their consistency in images spanning the full range of observed rotation phases on all three days and in echo power spectra obtained on opposite sides of Bacchus on March 22 and 24.

Estimating the COM time delays required correcting for echo drift through the ephemeris. An echo's time delay $\tau(t)$ is related to the Doppler frequency $\nu(t)$ by

$$d\tau(t)/dt = -\nu(t)/F_{\text{TX}}, \quad (5)$$

where F_{TX} is the transmitter frequency. Thus, a Doppler correction $\Delta\nu = 1$ Hz translates into a delay drift rate of $d\Delta\tau(t)/dt = -0.423 \mu\text{s/hr}$. We estimated Doppler corrections of -2 Hz from 150 m x 1 Hz images on March 22 and -1.5 and -3 Hz from 75 m x 1 Hz images on March 24 and 29, respectively (Table III), giving rates of 0.9, 0.6, and 1.3 $\mu\text{s/hr}$ that were used to shift single looks into delay registration with each other prior to summing. We estimate the COM time delay to be within the far lobe near its leading edge. Each of our summed images spans $\sim 10^\circ$ of rotational phase, an interval chosen as a trade-off that keeps rotational smear to less than 1 pixel.

Optical lightcurves of Bacchus were obtained by one of us (P. Pravec) at Ondrejov Observatory on 8 nights between 1996 March 25-26 and April 17-18 and are summarized in Table V. The lightcurve data reduction and analysis follows that used by Pravec *et al.* (1996) but a detailed description is presented elsewhere (Pravec *et al.* 1998). We used delay-Doppler images

and the lightcurves in the Bacchus shape inversion to find shapes that are consistent with both data sets, following the approach applied to 4769 Castalia by Hudson *et al.* (1997).

3. RESULTS

Doppler-only (cw) observations

Figure 2 shows 2-Hz-resolution echo power spectra from each day. The disc-integrated radar cross sections, circular polarization ratios, and bandwidths are consistent on all three days and are summarized in Table VI. Weighted sums of all the observations give a radar cross section $\sigma_{OC} = 0.12^{+0.06}_{-0.02} \text{ km}^2$ and a circular polarization ratio $\mu_C = 0.21 \pm 0.012$. Our uncertainties are estimated standard errors and the error interval on σ_{OC} is asymmetric to accommodate possible pointing errors. The circular polarization ratio is less than those observed from other radar-detected NEAs, which have a mean and rms dispersion of 0.35 ± 0.27 (Ostro *et al.* 1991b, Benner *et al.* 1997), indicating that the near-surface of Bacchus is somewhat smoother at centimeter-to-decimeter spatial scales than that of the average radar-detected near-Earth asteroid. The raw resolution of 1.95 Hz provides a coarse estimate of the maximum bandwidth of 6 Hz from a weighted sum of all the cw spectra, giving a lower bound on the maximum pole-on breadth of $\sim 0.9 \text{ km}$.

The March 22 OC spectrum reveals a statistically significant central dip that does not appear in spectra obtained on the other two days when the average rotation phases were displaced by about 70° and 60° , respectively, relative to the average rotation phase on March 22. The dip suggests a central deficit of mass and is reminiscent of central dips seen at certain rotation phases in echo power spectra of NEAs 1627 Ivar (Ostro *et al.* 1990a), 4769 Castalia (Ostro *et al.* 1990b),

and 6178 (1986 DA) (Ostro *et al.* 1991a), and in main-belt asteroid 216 Kleopatra (Mitchell *et al.* 1995).

Delay-Doppler images

Figures 3, 4, and 5 show high-resolution delay-Doppler images from each day. The March 22 images (Fig. 3) show a bimodal distribution of echo power in all panels but the third. The March 24 and 29 images (Figs. 5 and 6), which achieve stronger SNRs (Table VI) and better spatial resolution (Table II) than the March 22 images, also show a bimodal distribution of echo power in images spanning about 80° of rotation phase on the two days.

Images obtained on March 29 (Fig. 5) show Bacchus close to an “end-on” orientation when its two components were nearly parallel to the radar line-of-sight. In contrast, a March 22 image at nearly the same average rotation phase (Fig. 3, middle panel) shows a 7-sigma echo from the near component but no apparent echo from the far component, suggesting that the far component was being partially occulted and that the subradar latitude was close to equatorial on that day. The consistent bandwidths that are observed at comparable average rotation phases in images on the first and third days also argue that the subradar latitude was within a few tens of degrees of Bacchus’ equator throughout the experiment despite $\sim 30^\circ$ of sky motion between March 22 and 29.

Echo power in the end-on images obtained on March 29 (Fig. 5) is strongest at the leading edges of each component and diminishes as a function of increasing time delay. This is the delay-Doppler echo power distribution expected from two adjacent, rounded targets (Ostro *et al.* 1990b) and is evidence for a shape bifurcation.

Figure 6 compares echo power spectra from March 22 and 24 that were obtained on

opposite sides of Bacchus. The spectra have similar edge frequencies and shapes that are consistent with an object that is not substantially asymmetric. The central dip of echo power in the spectra is evidence for a central mass deficit on both sides of Bacchus and thus for a bifurcated shape.

Table VI lists the maximum delay and Doppler dispersions of Bacchus, which we obtained using contiguous cells with echo power exceeding the 2-sigma level. The maximum delay extent of ~ 0.6 km is seen when Bacchus is oriented nearly end-on, but if we assume that the radar illuminates only one-half of the far lobe, which would be true if the lobe were a sphere, then the far lobe's observed delay extent of ~ 4 range gates on March 29 suggests that lobe's true range extent may be ~ 8 range gates. If so, then Bacchus' maximum pole-on dimension may be ~ 13 range gates or close to 1 km, which is consistent with D_{\max} estimated from coarser-resolution cw spectra obtained on March 24.

Figure 7 shows how the radar and optical geometric albedos of Bacchus depend on its areal diameter. The figure also indicates representative values of p_v for principal taxonomic classes and condenses information about the distribution of estimates of other asteroid radar albedos. We adopt a lower bound of $D_{\max} \geq 0.6$ km from the maximum delay dispersion, which (let us equate D_{\max} to D_{area}) gives upper bounds on the geometric and radar albedos of 0.7 and 0.42, bounds that do not exclude Bacchus from any taxonomic class. However, unless D_{area} is close to ~ 1.8 km, which the radar images suggest is unlikely, then the optical geometric and radar albedos of Bacchus are probably too large to be consistent with the C classification that was suggested by Lazzarin *et al.* (1997).

Figure 8 shows Bacchus' ecliptic coordinates when it was observed with radar and when it was observed photometrically. Bacchus moved 102° between March 22, when radar observations

suggest the sub-Earth latitude was close to equatorial, and April 18, when photometric observations concluded. The final five of the eight lightcurves (April 6-7 to 17-18), which were weighted more heavily in Pravec *et al.*'s fit, were obtained at an average angular displacement of $\sim 90^\circ$ relative to Bacchus' position on March 22, suggesting that the sub-Earth latitude was within a few tens of degrees of a pole on April 6-18. The lightcurve amplitude decreased from 0.45 to 0.2 magnitudes as the solar phase angle decreased from 95° to 25° between late March and mid-April, which is also consistent with a sub-Earth latitude that was approaching a pole. Taken together, these lines of evidence suggest that Bacchus' spin vector is pointed to within a few tens of degrees of ecliptic latitude $\beta \sim -25^\circ$ and ecliptic longitude $\lambda \sim 0^\circ$.

4. BACCHUS' SHAPE AND COMPOSITION

Is Bacchus a double asteroid? If Bacchus consists of two identical, uniform-density spheres bound to each other by just their mutual gravity, then their density ρ would satisfy:

$$\rho \geq \rho_{\text{crit}} = 12\pi/GP^2 = 0.2 \text{ g cm}^{-3}$$

(where G is the gravitational constant and P is the true rotation period), a lower limit that is less than 10% of the densities of all known classes of meteorites (Dodd 1981). On the other hand, our data lack sufficient delay-Doppler resolution, echo strength, and geometric leverage to let us determine directly from the images whether the two components touch. Therefore, we modeled Bacchus as two homogeneous spheres of equal density and radius and used Kepler's 3rd law to place upper bounds on the densities that are consistent with the asteroid's rotation period. Figure 9 plots the surface-to-surface separation between the lobes as a function of diameter for a range of plausible densities. For this simple model, the lower bound on the lobe diameters and the upper bound on their surface-to-surface separation from the 75 m x 1

Hz images on March 24 and 29 would constrain the density of the co-orbiting lobes to be less than $\sim 0.5 \text{ g cm}^{-3}$, much less than the density of $\sim 3.6 \text{ g cm}^{-3}$ of plausible Bacchus meteorite analogues, the ordinary chondrites (Dodd 1981), and also less than the lowest estimated asteroid density of $\sim 1.3 \pm 0.2 \text{ g cm}^{-3}$ for 253 Mathilde (Veeverka *et al.* 1997, Yeomans *et al.* 1997). Consequently, the unrealistically low densities that the model implies constitute strong evidence against a binary configuration.

Given sufficient echo strengths and orientational coverage of the surface, a sequence of delay-Doppler images can be used to reconstruct an asteroid's shape and spin state (Hudson 1993; Hudson and Ostro 1994, 1995). We found that only the March 24 and 29 $0.5 \mu\text{s} \times 1 \text{ Hz}$ images have sufficient SNR for this purpose. Those sequences span 2.2 h and 1.4 h, respectively, and represent somewhat less than 90° of total rotation phase coverage, but additional constraints in the form of cw spectra from March 22, 24, and 29 and optical lightcurves from March 26, 27-28, March 31-April 1, and April 6-7, 7-8, 15-16, 16-17, and 17-18 are also available. The radar data include nearly end-on and broadside orientations, and the relationship between delay and Doppler dispersions at these orientations, coupled with Bacchus' $\sim 30^\circ$ of sky motion between March 22 and 29 (and $\sim 100^\circ$ of sky motion between March 22 and the end of lightcurve observations on April 18) constrain the pole and gross shape. It is possible to investigate the types of shapes and spin states that can account for the bifurcated appearance of many of the delay-Doppler images and Doppler spectra and for the overall evolution of the lightcurves (Hudson *et al.* 1997). However, due to the lack of sufficient resolution we do not expect this data set to support a detailed or unique shape model.

We began with a grid search over all possible pole directions using both a biaxial ellipsoid model and a two-lobe model, following the approach adopted in the inversion of the Castalia

radar data (Hudson and Ostro 1994). These shapes and the rotation period were free parameters for every candidate pole direction. In this manner we identified the region within a few tens of degrees of ecliptic longitude $\lambda = 20^\circ$ and ecliptic latitude $\beta = -20^\circ$ as that which gave the best fits.

Each model is specified by 256 vertex shape parameters. Since most of the asteroid's surface was not imaged we constrained the spin state to correspond to a homogeneous body in principal axis rotation. For the two-lobe model, deviations from the spherical shapes were penalized until χ^2 began to increase significantly, where a 2% change in χ^2 is significant at the one standard deviation level for these data, which contain 369 independent measurements of radar echo and optical lightcurves. For the one-lobe model, concavities were penalized in a similar manner.

The shape models and fits to the delay-Doppler images, cw spectra, and lightcurves are shown in Figs. 10, 11, and 12, and physical properties derived from the shape models are summarized in Table VII. The two shape models provide a statistically equivalent goodness of fit (χ^2). Both models have a central concavity or “waist” that is also evident in the modeled images, a modestly asymmetric shape, and similar maximum dimensions, effective diameters, and aspect ratios. The rotation periods and pole directions are consistent with each other within their standard errors and favor retrograde rotation a bit more than direct rotation. The sidereal rotation period is consistent with the value estimated by Pravec from his lightcurves.

The effective diameters of 0.63 and 0.67 km derived from the single- and two-lobe shape models imply unusually large radar ($\hat{\sigma} \sim 0.3$) and optical geometric ($p_v \sim 0.6$) albedos. Due in part to our experience with modeling other asteroids, and because of the low SNR, coarse delay-Doppler resolution, and incomplete coverage of Bacchus' surface in the radar images, we estimate standard errors in Bacchus' effective diameter of $^{+20\%}_{-10\%}$ that propagate into standard

errors for $\hat{\sigma}$ and p_v , giving $\hat{\sigma} \approx 0.33^{+0.25}_{-0.11}$ and $p_v = 0.56^{+0.12}_{-0.18}$ for the one-lobe model and $\hat{\sigma} \approx 0.28^{+0.22}_{-0.10}$ and $p_v = 0.49^{+0.10}_{-0.14}$ for the two-lobe model.

The two shape models provide a sense of the bounds on the degree of bifurcation of the shape of Bacchus. The inversion indicates that Bacchus' shape is at least as nonconvex and bifurcated as that of the single lobe model and perhaps as nonconvex and bifurcated as the two-lobe model. Let us adopt the more conservative single-lobe model as our working model and explore its implications.

The measured and synthetic lightcurves for the single-lobe model (Fig. 12) have an rms residual of 0.04 mag (and a comparable value for the two-lobe model) that may result from shape, inhomogeneity, or systematic effects. For comparison, the lightcurve residuals for the Gaspra and Ida data sets, where the shape models are based on Galileo images, are ~ 0.05 mag (Simonelli *et al.* 1995, 1996). If we let the Bacchus models get very irregular by relaxing the terms in the estimation that penalize concavities (Hudson and Ostro 1994), we can improve the fit to the lightcurve features but it is not clear that the resulting changes to the shape models have any relation to Bacchus' true shape.

The optical geometric albedo of Bacchus is among the largest estimated for any asteroid. Even within the one-sigma lower bound of $p_v \sim 0.4$, Bacchus is a bright object at optical wavelengths. The only other NEAs with comparable geometric albedos are 2201 Oljato ($p_v \sim 0.5$, taxonomic class uncertain; Veeder *et al.* 1989), 3103 Eger ($p_v \sim 0.6$, E-class; Veeder *et al.* 1989), and 3908 (1980 PA) ($p_v \sim 0.6$, V-class; Cruikshank *et al.* 1991), whose albedos were estimated using the standard thermal model (Morrison and Lebofsky 1979); and 6489 Golevka ($p_v \sim 0.6$, Mottola *et al.* 1997), whose albedo was estimated using the fast rotating model. (However, more recent work suggests the albedos of Oljato and Eger may be lower; see McFadden *et al.* 1993 and

Benner *et al.* 1997.) The optical geometric albedo of Bacchus is ~50% larger than the largest NEA S-class albedos that have been reported (1566 Icarus and 3199 Nefertiti; Veeder *et al.* 1989) and about a factor of three larger than the albedo of Q-class NEA 1862 Apollo (Lebofsky *et al.* 1981).

Bacchus' optical geometric and single scattering albedos are comparable to those estimated for Golevka (Mottola *et al.* 1997), which has a visible spectrum between 0.5 and 1.0 μm that closely resembles that of Bacchus (Binzel *et al.* 1996, Hicks *et al.* 1998), suggesting that Golevka and Bacchus may have similar compositions. Mottola *et al.* (1997) and Hicks *et al.* (1998) tentatively assign Golevka to the V-class, although its optical spectrum is also consistent with the Q-S continuum described by Binzel *et al.* (1996). However, even at the 1-sigma lower limit of $p_v \sim 0.4$, the optical albedo of Bacchus exceeds $p_v = 0.34$ estimated for V-class object 4 Vesta (using the mean diameter recently determined by Thomas *et al.* 1997). Unfortunately, infrared spectra that might show the 1.25-micron plagioclase absorption diagnostic of V-class objects are not available for either Bacchus or Golevka.

Bacchus' nominal radar albedo is third largest known and is exceeded by only the radar albedos of M-class objects 6178 (1986 DA) ($\hat{\sigma}_{oc} \sim 0.58$, Ostro *et al.* 1991a) and 216 Kleopatra ($\hat{\sigma}_{oc} \sim 0.44$, Mitchell *et al.* 1995), and it is comparable to that of NEA 3199 Nefertiti ($\hat{\sigma}_{oc} \sim 0.32$, Ostro *et al.* 1991a), the maximum estimated for the S-class. The 1-sigma lower limit of 0.22 exceeds the radar albedos of ~90% of radar-detected asteroids and establishes that Bacchus is a radar-bright object. High $\hat{\sigma}_{oc}$ implies that Bacchus has a denser surface (either more metal, lower porosity, or both) than that of the average radar-detected near-Earth or main-belt asteroid.

The polarization ratio of Bacchus indicates that most of the echo power is from single

backscattering. Consequently, $\hat{\sigma}_{oc}$ can be treated to first-order as an approximation to the normal reflectance R (justified because $g \sim 1.4$), which (through Eq. 3) gives a surface bulk density $d \sim 3.3^{+1.4}_{-0.7} \text{ g cm}^{-3}$. Figure 13 shows R as a function of porosity for various types of meteorites. The normal reflectance of Bacchus overlaps estimates for near-zero porosity ordinary and carbonaceous chondrites and basaltic achondrites, and with $\sim 40\%$ porosity stony-iron and $\sim 60\%$ porosity iron regoliths, although carbonaceous chondrite, stony-iron, and iron compositions are excluded by visible spectroscopy. A nearly regolith-free ordinary chondrite composition is consistent with inferences about Bacchus' composition from its optical spectrum (Binzel *et al.* 1996, Hicks *et al.* 1998), and a nearly regolith-free basaltic achondrite composition is consistent with a V-classification. However, if Bacchus is a member of the Q-S continuum with an ordinary chondrite composition (Binzel *et al.* 1996, Hicks *et al.* 1998), then the optical geometric albedo may indicate a discrepancy because it is much higher than those estimated for other Q-S class objects. The apparent discrepancy may be resolved if Bacchus is a V-class object and if the radar and optical geometric albedos and optical and infrared spectra of 1980 PA and Golevka are shown to be similar to those of Bacchus. What is clear is that the high radar and optical albedos indicate that Bacchus is an outlier among the near-Earth asteroids.

5. DISCUSSION

How did the shape of Bacchus originate? One possibility is that the two lobes once were separate objects in orbit about their mutual center of mass, perhaps produced as adjacent fragments either in a catastrophic collision of a larger parent body (Hartmann 1979, Durda 1996, Doressoundiram *et al.* 1997), or through disruption but not dispersal of an originally intact

fragment (Love and Ahrens 1997, Asphaug *et al.* 1998). Subsequently the lobes collided, either because gravitational perturbations experienced during a close encounter with Earth or Venus increased the eccentricity of the binary's orbit sufficiently for a collision (Chauvineau *et al.* 1995), or because tidal friction between the components caused the semimajor axis to decay due to Bacchus' retrograde rotation (which would be true if one of the two lobes were a direct rotator). Alternatively, if Bacchus consists of a loose gravitationally-bound aggregate (or "rubble pile"), then planetary tides may have distorted it to its present shape during passage within the Roche zone of Earth or Venus (Bottke and Melosh 1996a,b; Solem and Hills 1996).

Bacchus' long rotation period raises the question of whether it is in a non-principal axis rotation state. We estimate the time scale for damping to principal axis rotation from

$$\tau_D \approx (P/C)^3/D_{\text{eff}}^2, \quad (6)$$

where P is the sidereal period in hours, D_{eff} is in km, τ_D is in billions of years, and C is a parameter that depends on the material properties of the asteroid (Harris 1994). Using $C = 17 \pm 2.5$ (Harris 1994), $P = 15$ h, and $D_{\text{eff}} = 0.63$ km, we obtain a time scale $\tau_D = 1.73^{+1.06}_{-0.58} \times 10^9$ y. Thus it is conceivable that Bacchus may be in a non-principal axis spin state but we find no evidence for it.

How abundant are bifurcated near-Earth asteroids? The answer to this question has important implications for understanding the collisional evolution of the near-Earth and main-belt asteroid populations (Ostro *et al.* 1990a). To date, delay-Doppler images and their shape reconstructions have been reported for three objects: 1620 Geographos (Ostro *et al.* 1995a, 1996; Hudson and Ostro 1997), 4179 Toutatis (Ostro *et al.* 1995b, Hudson and Ostro 1995), and 4769 Castalia (Ostro *et al.* 1990a, Hudson and Ostro 1994, Hudson *et al.* 1997). Of these, Castalia and Toutatis show evidence for a bifurcated shape and Geographos shows a central indentation, but

only Castalia has a mass distribution that strongly suggests a contact binary object. The small number of detailed shape models that are presently available will grow significantly over the next decade.

The next opportunity to obtain echoes from Bacchus at least as strong as those reported here is in 2015 when the estimated SNR/date at Arecibo should be close to 100. The best Bacchus opportunities in the next fifty years will occur at Arecibo in 2024 and 2043 at estimated SNRs/date of ~ 700 and ~ 5000 , respectively, that should be strong enough for a detailed three-dimensional shape reconstructions.

ACKNOWLEDGMENTS

We thank Peter Ford and an anonymous reviewer for thoughtful reviews. L. A. M. Benner was supported as a Research Associate of the National Research Council. Work at Washington State University was supported, in part, by NASA grant NAGW 4636. Part of this research was conducted at the Jet Propulsion Laboratory, California Institute of Technology, under contract with the National Aeronautics and Space Administration.

REFERENCES

- Asphaug, E., S. J. Ostro, R. S. Hudson, D. J. Scheeres, and W. Benz 1998. Disruption of kilometre-sized asteroids by energetic collisions. *Nature* **393**, 437-440.
- Benner, L. A. M., S. J. Ostro, J. D. Giorgini, R. F. Jurgens, D. L. Mitchell, R. Rose, K. D. Rosema, M. A. Slade, R. Winkler, D. K. Yeomans, D. B. Campbell, J. F. Chandler, and I. I. Shapiro 1997. Radar detection of near-Earth asteroids 2062 Aten, 2101 Adonis, 3103 Eger, 4544 Xanthus, and 1992 QN. *Icarus* **130**, 296-312.
- Binzel, R. P., S. J. Bus, T. H. Burbine, and J. M. Sunshine 1996. Spectral properties of near-Earth asteroids: Evidence for sources of ordinary chondrite meteorites. *Science* **273**, 946-948.
- Bottke, W. F., and H. J. Melosh 1996a. Formation of asteroid satellites and doublet craters by planetary tidal forces. *Nature* **381**, 51-53.
- Bottke, W. F., and H. J. Melosh 1996b. Binary asteroids and the formation of doublet craters. *Icarus* **124**, 372-391.
- Campbell, M. J., and J. Ulrichs 1969. Electrical properties of rocks and their significance for lunar radar observations. *J. Geophys. Res.* **74**, 5867-5881.
- Chamberlin, A. B., D. K. Yeomans, P. W. Chodas, J. D. Giorgini, R. A. Jacobson, M. S. Keesey, J. H. Lieske, S. J. Ostro, E. M. Standish, and R. N. Wimberly 1997. JPL solar system dynamics WWW site. *Bull. Am. Astron. Soc.* **29**, 1014. [Abstract]
- Chauvineau, B., P. Farinella, and A. W. Harris 1995. The evolution of Earth-approaching binary asteroids: A Monte Carlo dynamical model. *Icarus* **115**, 36-46.
- Dodd, R. T. 1981. *Meteorites*. Cambridge University Press, Cambridge.
- Doressoundiram, A., P. Paolicchi, A. Verlicchi, and A. Cellino 1997. The formation of binary

- asteroids as outcomes of catastrophic collisions. *Planet. Space Sci.* **45**, 757-770.
- Durda, D. D. 1996. The formation of asteroidal satellites in catastrophic collisions. *Icarus* **120**, 212-219.
- Garvin, J. B., J. W. Head, G. H. Pettengill, and S. H. Zisk 1985. Venus global radar reflectivity and correlations with elevation. *J. Geophys. Res.* **90**, 6859-6871.
- Hapke, B. W. 1981. Bidirectional reflectance spectroscopy. I. Theory. *J. Geophys. Res.* **86**, 3039-3054.
- Hapke, B. W. 1984. Bidirectional reflectance spectroscopy. III. Correction for macroscopic roughness. *Icarus* **59**, 41-59.
- Hapke, B. W. 1986. Bidirectional reflectance spectroscopy. IV. The extinction coefficient and the opposition effect. *Icarus* **67**, 264-280.
- Harris, A. W. 1994. Tumbling asteroids. *Icarus* **107**, 209-211.
- Hartmann, W. K. 1979. Diverse puzzling asteroids and a possible unified explanation. In *Asteroids* (T. Gehrels, Ed.), pp. 466-479. University of Arizona Press, Tucson.
- Helfenstein, P., and J. Veverka 1989. Physical characterization of asteroid surfaces from photometric analyses. In *Asteroids II* (R. P. Binzel, T. Gehrels, and M.S. Matthews, Eds.), pp. 557-593. University of Arizona Press, Tucson.
- Hicks, M. D., U. Fink, and W. M. Grundy 1998. The unusual spectra of 15 near-Earth asteroids and extinct comet candidates. *Icarus* **133**, 69-78.
- Hudson, S. 1993. Three-dimensional reconstruction of asteroids from radar observations. *Remote Sensing Rev.* **8**, 195-203.
- Hudson, R. S., and S. J. Ostro 1994. Shape of asteroid 4769 Castalia (1989 PB) from inversion of radar images. *Science* **263**, 940-943.

- Hudson, R. S., and S. J. Ostro 1995. Shape and non-principal axis spin state of asteroid 4179 Toutatis. *Science* **270**, 84-86.
- Hudson, R. S., and S. J. Ostro 1997. Recent radar modeling results: 1620 Geographos and 4179 Toutatis. *Bull. Am. Astron. Soc.* **29**, 966. [Abstract]
- Hudson, R. S., S. J. Ostro, and A. W. Harris 1997. Constraints on the spin state and Hapke parameters of asteroid 4769 Castalia using lightcurves and a radar-derived shape model. *Icarus* **130**, 165-176.
- Kelly, J. M., J. O. Stenoien, and D. E. Isbell 1953. Wave-guide measurements in the microwave region on metal powders suspended in paraffin wax. *J. Appl. Phys.* **24**, 258-262.
- Kendall, M., and A. Stuart 1979. *The Advanced Theory of Statistics. Volume 2. Inference and Relationship*. MacMillan, New York.
- Kowal, C. 1977. *IAU Circ.* 3066.
- Lazzarin, M., M. Di Martino, M. A. Barucci, A. Doressoundiram, and M. Florczak 1997. Compositional properties of near-Earth asteroids: Spectroscopic comparison with ordinary chondrite meteorites. *Astron. Astrophys.* **327**, 388-391.
- Lebofsky, L. A., G. J. Veeder, G. H. Rieke, M. J. Lebofsky, D. L. Matson, C. Kowal, C. G. Wynn-Williams, and E. E. Becklin 1981. The albedo and diameter of 1862 Apollo. *Icarus* **48**, 335-338.
- Love, S. G., and T. J. Ahrens 1997. Origin of asteroid rotation rates in catastrophic impacts. *Nature* **386**, 154-156.
- McFadden, L. A., A. L. Cochran, E. S. Barker, D. P. Cruikshank, and W. K. Hartmann 1993. The enigmatic object 2201 Oljato: Is it an asteroid or an evolved comet? *J. Geophys. Res.* **98**, 3031-3041.

- Mitchell, D. L., S. J. Ostro, K. D. Rosema, R. S. Hudson, D. B. Campbell, J. F. Chandler, and I. I. Shapiro 1995. Radar observations of asteroids 7 Iris, 9 Metis, 12 Victoria, 216 Kleopatra, and 654 Zelinda. *Icarus* **118**, 105-131.
- Mitchell, D. L., S. J. Ostro, R. S. Hudson, K. D. Rosema, D. B. Campbell, R. Vélez, J. F. Chandler, I. I. Shapiro, J. D. Giorgini, and D. K. Yeomans 1996. Radar observations of asteroids 1 Ceres, 2 Pallas, and 4 Vesta. *Icarus* **124**, 113-133.
- Morrison, D., and L. A. Lebofsky 1979. Radiometry of asteroids. In *Asteroids* (T. Gehrels, Ed.), pp. 184-205. University of Arizona Press, Tucson.
- Mottola, S., A. Erikson, A. W. Harris, G. Hahn, G. Neukum, M. W. Buie, W. D. Sears, A. W. Harris, D. J. Tholen, R. J. Whiteley, P. Magnusson, J. Piironen, T. Kwiatkowski, W. Borczyk, E. S. Howell, M. D. Hicks, R. Fevig, Yu. N. Krugly, F. P. Velichko, V. G. Chiorny, N. M. Gaftonyuk, M. Di Martino, P. Pravec, L. Sarounová, M. Wolf, W. Worman, J. K. Davies, H.-J. Schober, and W. Pych 1997. Physical model of near-Earth asteroid 6489 Golevka (1991 JX) from optical and infrared observations. *Astron. J.* **114**, 1234-1245.
- Nielson, L. E. 1974. The permittivity of suspensions and two-phase mixtures. *J. Phys. D.: Appl. Phys.* **7**, 1549-1554.
- Ostro, S. J. 1993. Planetary radar astronomy. *Rev. Mod. Phys.* **65**, 1235-1279.
- Ostro, S. J., D. B. Campbell, and I. I. Shapiro 1985. Mainbelt asteroids: Dual-polarization radar observations. *Science* **229**, 442-446.
- Ostro, S. J., D. B. Campbell, A. A. Hine, I. I. Shapiro, J. F. Chandler, C. L. Werner, and K. D. Rosema 1990a. Radar images of asteroid 1627 Ivar. *Astron. J.* **99**, 2012-2018.
- Ostro, S. J., J. F. Chandler, A. A. Hine, K. D. Rosema, I. I. Shapiro, and D. K. Yeomans 1990b.

- Radar images of asteroid 1989 PB. *Science* **248**, 1523-1528.
- Ostro, S. J., D. B. Campbell, J. F. Chandler, A. A. Hine, R.S. Hudson, K. D. Rosema, and I. I. Shapiro 1991a. Asteroid 1986 DA: Radar evidence for a metallic composition. *Science* **252**, 1399-1404.
- Ostro, S. J., D. B. Campbell, J. F. Chandler, I. I. Shapiro, A. A. Hine, R. Velez, R. F. Jurgens, K. D. Rosema, R. Winkler, and D. K. Yeomans 1991b. Asteroid radar astrometry. *Astron. J.* **102**, 1490-1502.
- Ostro, S. J., D. B. Campbell, R. A. Simpson, R. S. Hudson, J. F. Chandler, K. D. Rosema, I. I. Shapiro, E. M. Standish, R. Winkler, D. K. Yeomans, R. Velez, and R. M. Goldstein 1992. Europa, Ganymede, and Callisto: New radar results from Arecibo and Goldstone. *J. Geophys. Res.* **97**, 18,227-18,244.
- Ostro, S. J., K. D. Rosema, R. S. Hudson, R. F. Jurgens, J. D. Giorgini, R. Winkler, D. K. Yeomans, D. Choate, R. Rose, M. A. Slade, S. D. Howard, and D. L. Mitchell 1995a. Extreme elongation of asteroid 1620 Geographos from radar images. *Nature* **375**, 474-477.
- Ostro, S. J., R. S. Hudson, R. F. Jurgens, K. D. Rosema, D. B. Campbell, D. K. Yeomans, J. F. Chandler, J. D. Giorgini, R. Winkler, R. Rose, S. D. Howard, M. A. Slade, P. Perillat, and I. I. Shapiro 1995b. Radar images of asteroid 4179 Toutatis. *Science* **270**, 80-83.
- Ostro, S. J., R. F. Jurgens, K. D. Rosema, R. S. Hudson, J. D. Giorgini, R. Winkler, D. K. Yeomans, D. Choate, R. Rose, M. A. Slade, S. D. Howard, D. J. Scheeres, and D. L. Mitchell 1996. Radar observations of asteroid 1620 Geographos. *Icarus* **121**, 46-66.
- Pettengill, G. H., P. G. Ford, and B. D. Chapman 1988. Venus: Surface electromagnetic properties. *J. Geophys. Res.* **93**, 14881-14892.

- Pravec, P., L. Sarounova, and M. Wolf 1996. Lightcurves of 7 near-Earth asteroids. *Icarus* **124**, 471-482.
- Pravec, P., M. Wolf., and L. Sarounova 1998. Lightcurves of 26 near-Earth asteroids. *Icarus*, in press.
- Simonelli, D. P., J. Veverka, P. C. Thomas, P. Helfenstein, and M. J. S. Belton 1995. Analysis of Gaspra lightcurves using Galileo shape and photometric models. *Icarus* **114**, 387-402.
- Simonelli, D. P., J. Veverka, P. C. Thomas, P. Helfenstein, B. T. Carcich, and M. J. S. Belton 1996. Ida lightcurves: Consistency with Galileo shape and photometric models. *Icarus* **120**, 38-47.
- Solem, J. C., and J. G. Hills 1996. Shaping of Earth-crossing asteroids by tidal forces. *Astron. J.* **111**, 1382-1387.
- Tedesco, E. F. 1989. Asteroid magnitudes, UBV colors, and IRAS albedos and diameters. In *Asteroids II* (R. P. Binzel, T. Gehrels, and M. S. Matthews, Eds.), pp. 1090-1138. University of Arizona Press, Tucson.
- Thomas, P. C., R. P. Binzel, M. J. Gaffey, A. D. Storrs, E. N. Wells, and B. H. Zellner 1997. Impact excavation on asteroid 4 Vesta: Hubble Space Telescope results. *Science* **277**, 1492-1495.
- Ulaby, F. T., T. H. Bengal, M. C. Dobson, J. R. East, J. B. Garvin, and D. L. Evans 1990. Microwave dielectric properties of dry rocks. *IEEE Trans. Geosci. Remote Sens.* **28**, 325-336.
- Veverka, J., P. Thomas, A. Harch, B. Clark, J. F. Bell III, B. Carcich, J. Joseph, C. Chapman, W. Merline, M. Robinson, M. Malin, L. A. McFadden, S. Murchie, S. E. Hawkins III, R. Farquhar, N. Izenberg, and A. Cheng 1997. NEAR's flyby of 253 Mathilde: Images of a C

asteroid. *Science* **278**, 2109-2114.

Yeomans, D. K., J.-P. Barriot, D. W. Dunham, R. W. Farquhar, J. D. Giorgini, C. E. Helfrich, A. S.

Konopliv, J. V. McAdams, J. K. Miller, W. M. Owen Jr., D. J. Scheeres, S. P. Synnott, and

B. G. Williams 1997. Estimating the mass of asteroid 253 Mathilde from tracking data

during the NEAR flyby. *Science* **278**, 2106-2109.

Zellner, B. 1979. Asteroid taxonomy and the distribution of the compositional types. In *Aster-*

oids (T. Gehrels, Ed.), pp. 783-806. University of Arizona Press, Tucson.

TABLE I
Optically Determined Physical Properties

Property	Value
H (mag)	17.25 ± 0.2^b
Class	Q^a, C^c
P (h)	14.904 ± 0.003^b
Δm	$0.2 - 0.4^b$

Note. H is the absolute visual magnitude, class refers to the taxonomic class, P is the synodic rotation period in hours, and Δm indicates the range of observed lightcurve amplitudes.

^a Hicks *et al.* (1998).

^b Pravec *et al.* (1998).

^c Lazzarin *et al.* (1997).

TABLE II

Radar Observations

Date	RA (°)	DEC (°)	Distance (AU)	POS motion (°)	P_{TX} (kW)	Runs	Δt (UTC hours)	Setup	$\Delta\phi$ (°)
1996 March 22	313.2	59.0	0.087	0.8	491	22	17.62 - 18.87	1.95 Hz	0 - 28
						13	19.52 - 20.21	11.0 μ s x 5.6 Hz	46 - 62
						9	20.44 - 20.89	7.00 μ s x 5.9 Hz	68 - 78
						36	21.62 - 00.01	1.00 μ s x 1.0 Hz	96 - 154
1996 March 24	301.0	62.7	0.080	1.0	491	19	17.26 - 18.31	1.95 Hz	71 - 96
						12	19.14 - 19.72	0.25 μ s x 0.5 Hz	116 - 130
						44	20.09 - 22.32	0.50 μ s x 1.0 Hz	139 - 193
						10	22.75 - 23.25	7.00 μ s x 5.9 Hz	204 - 215
1996 March 29	249.1	64.2	0.069	0.9	251	27	16.41 - 17.96	1.95 Hz	69 - 106
						31	18.22 - 19.60	0.50 μ s x 1.0 Hz	113 - 146

Note. Right ascension, declination, and distance are given at the middle of each day's observations. Target plane-of-sky (POS) motion between start of reception of the first echo and end of reception of the last echo on each day is indicated. Total POS motion between the beginning of the experiment on March 22 and the end on March 29 was $\sim 30^\circ$. P_{TX} is the average transmitter power on each day. The number of transmit-receive cycles (runs) is listed in the sixth column. Δt is the interval spanned by each type of observation on each date. We list the raw cw frequency resolutions and the raw delay-Doppler resolutions in the ninth column. $\Delta\phi$ is the rotation phase coverage observed with each setup, where we have adopted the rotation period in Table I and the start of reception at 17:37:31 UTC on 1996 March 22 defines the zero-phase epoch.

TABLE III

Radar Astrometry

Date	UTC Epoch	Type	OSOD Solution	Correction	Measurement	Uncertainty
1996 March 22	18:00:00	Doppler	4	0 Hz	384,093.2 Hz	2 Hz
	20:10:00	delay	4	-502 μ s	87,190,665 μ s	15 μ s
	22:50:00	delay	4	-495 μ s	86,769,151 μ s	2 μ s
	22:50:00	Doppler	4	-2 Hz	371,573.7 Hz	2 Hz
1996 March 24	17:50:00	Doppler	6	-1.5Hz	324,347 Hz	2 Hz
	23:00:00	delay	6	+56 μ s	79,562,896 μ s	10 μ s
	22:10:00	delay	6	+59 μ s	79,673,366 μ s	1 μ s
1996 March 29	19:30:00	Doppler	6	-3 Hz	96,363 Hz	2 Hz

Note. Radar astrometry for echoes from Bacchus' estimated center of mass, received at the stated UTC epoch. The reference point for the Goldstone antenna is the intersection of the elevation and azimuth axes.

TABLE IV
Bacchus Orbit (OSOD-11)

Epoch (TDB)	1997 June 1.0
Eccentricity, e	0.34951388 (22)
Perihelion distance, q (AU)	0.70128437 (23)
Perihelion Passage (TDB)	1997 Mar 5.3487125 (113)
Argument of perihelion, ω (°)	55.1715731 (429)
Longitude of ascending node, Ω (°)	33.2539268 (357)
Inclination, i (°)	9.4326850 (116)

Note: These orbital elements are from a fit to optical and radar observations over the interval 1977 April 24 to 1997 May 17. A total of 221 optical astrometric observations are included. The radar data include four Doppler and four delay estimates in Table III. We used JPL ephemeris DE-405 (J2000). The rms residual for all 221 optical observations is 0.90 arc sec and the radar rms residuals are 1.3 Hz and 3.1 μ s. The angular orbital elements are referred to the ecliptic and mean equinox of J2000 and 3-sigma standard errors (in parentheses) are given in units of the last decimal place.

TABLE V

Lightcurve Observations

Date	RA (°)	DEC (°)	Distance (AU)	r (AU)	α (°)	Δt (UTC hours)
1996 Mar 26	290.5	64.6	0.077	0.989	94.5	0.23 - 3.68
1996 Mar 27-28	269.8	65.9	0.072	1.001	85.8	18.48 - 3.76
1996 Mar 31-Apr 1	227.5	58.1	0.068	1.025	65.8	19.12 - 3.54
1996 Apr 6-7	199.9	35.0	0.079	1.061	39.2	19.00 - 2.94
1996 Apr 7-8	197.8	31.9	0.083	1.067	36.1	19.02 - 1.67
1996 Apr 15-16	187.9	12.5	0.122	1.113	25.0	19.02 - 2.23
1996 Apr 16-17	187.2	10.9	0.128	1.118	24.9	19.56 - 2.01
1996 Apr 17-18	186.6	9.4	0.134	1.124	24.9	19.40 - 1.54

Note. Right ascension, declination, distances from Earth and the Sun, and the solar phase angle are given at the middle of each day's observations. Δt is the interval spanned by observations on each date.

TABLE VI
Disc-Integrated and Delay-Doppler Radar Properties

Date	Setup	OC SNR	B (Hz)	Delay Dispersion (km)	$\sigma_{OC}^{+50\% -20\%}$ (km ²)	μ_C	$\hat{\sigma}_{OC}$
<i>Disc-integrated properties</i>							
1996 March 22	1.95 Hz	32	4		0.10	0.20 ± 0.03	
1996 March 24	1.95 Hz	54	6		0.13	0.20 ± 0.02	
1996 March 29	1.95 Hz	57	4		0.13	0.23 ± 0.02	
whole experiment		80	6		0.12	0.21 ± 0.01	≤ 0.6
<i>Delay-Doppler properties</i>							
1996 March 22	1 μ s (150 m) x 1 Hz	8	4	0.6			
1996 March 24	0.5 μ s (75 m) x 1 Hz	15	4	0.6			
1996 March 29	0.5 μ s (75 m) x 1 Hz	15	4	0.6			

Note. Radar properties on each date, determined from weighted sums of cw spectra and delay-Doppler images. Setup gives the raw cw frequency and the raw delay-Doppler resolutions. OC SNR is the OC signal-to-noise ratio obtained from an optimally filtered weighted spectral sum. B is the echo bandwidth. The SNR for the images is computed from contiguous pixels with echo powers that exceed two standard deviations. σ_{OC} is the OC radar cross section; assigned uncertainties are the root sum square of systematic calibration errors that are estimated to be $^{+50\%}_{-20\%}$ of the radar cross section. $\hat{\sigma}_{OC}$ is the OC radar albedo and was computed from the 1-sigma upper limit in σ_{OC} and by equating D_{area} to 0.6 km.

TABLE VII

Physical Properties Derived from the Shape Models

Property	Single Lobe	Two Lobe
<i>Shape model</i>		
Volume (km ³)	0.13	0.16
D_{eff} (km)	$0.63^{+0.13}_{-0.06}$	$0.67^{+0.13}_{-0.07}$
Maximum extents (km)	1.11 x 0.53 x 0.50	1.03 x 0.57 x 0.57
p_v	$0.56^{+0.12}_{-0.18}$	$0.49^{+0.10}_{-0.14}$
<i>Spin Vector</i>		
λ (°)	24 ± 15	37 ± 15
β (°)	-26 ± 15	-26 ± 15
P_{sid} (h)	15 ± 0.2	15 ± 0.2
<i>Radar properties</i>		
ρ	0.40 ± 0.06	0.34 ± 0.06
n	$1.4^{+1}_{-0.4}$	$1.4^{+1}_{-0.4}$
R	$0.23^{+0.17}_{-0.08}$	$0.20^{+0.16}_{-0.07}$
$\hat{\sigma}$	$0.33^{+0.25}_{-0.11}$	$0.28^{+0.22}_{-0.10}$
<i>Hapke Parameters</i>		
w	0.60 ± 0.06	0.60 ± 0.06
g	-0.38 ± 0.04	-0.35 ± 0.04
θ (°)	23 ± 8	22 ± 8
B_0	(1.32)	(1.32)
h	(0.02)	(0.02)

Note. Physical parameters of Bacchus derived from the single-lobe and two-lobe shape models. D_{eff} is the effective diameter; uncertainties are estimated systematic standard errors. p_v is the optical geometric albedo computed from D_{eff} and Bacchus' absolute magnitude (Table I). λ and β are the ecliptic longitude and latitude of Bacchus' spin vector and P_{sid} is the sidereal rotation period. We adopt a radar scattering law with the form $\sigma_0 = \rho \cos^n \theta$, where ρ describes the reflectivity of the surface at normal incidence, n indicates the degree of specularity, and θ is the angle of incidence at a point on the surface. R is the Fresnel reflection coefficient at normal incidence, equal to $2\rho/(n+2)$. $\hat{\sigma}$ is the equivalent spherical radar albedo, equal to $2\rho/(n+1)$. w is the single scattering albedo, g is the single particle phase function, θ is the average slope of macroscopic roughness, B_0 is the opposition surge amplitude, and h is the opposition surge width (Hapke 1981,

1984, 1986). The lightcurve observations do not cover a large enough range of solar phase angles to independently estimate B_0 and h , so we have adopted representative values determined for S-class asteroids (Helfenstein and Veverka 1989). Uncertainties are estimated statistical standard errors and do not (except for D_{eff} , p_v , R , and $\hat{\sigma}$) reflect systematic errors.

FIGURE CAPTIONS

FIG. 1. Rotation phases of observations using synodic rotation periods of 14.90 h determined from optical lightcurves by Pravec *et al.* 1998. Rotation phase increases clockwise from 12 o'clock, where the start of reception of the first echo at 17:37:31 UTC on 1996 March 22 defines the zero-phase epoch. Concentric rings indicate observations on different days. A dashed line indicates the rotation phase when Bacchus' two lobes are aligned with the radar line-of-sight (see text).

FIG. 2. Echo power spectra from March 22, 24, and 29 at the raw 1.95-Hz resolution. Echo power is plotted in standard deviations versus Doppler frequency relative to the estimated frequency of echoes from the asteroid's center of mass. Solid and dashed lines denote echo power in the OC and SC polarizations. Rotational phase coverage is indicated as in Fig. 1.

FIG. 3. Sequence of five $1\ \mu\text{s}$ (150 m) \times 1 Hz images from March 22. Each image shows the distribution of echo power in standard deviations relative to Bacchus' estimated COM frequency and distance, which we estimate to be within the far lobe near its leading edge. The radar illuminates Bacchus from the top and range increases toward the bottom. Images in the top row are shown at the raw resolution and have been clipped at 0 and saturated at 5 standard deviations; those at the bottom have been smoothed and their contrast stretched to highlight pixels that contain echoes exceeding two standard deviations. Average rotation phases and midpoint epochs for each image are listed. Each panel shows about 8° of rotation and has been corrected for delay drift (see text).

FIG. 4. Sequence of $0.5 \mu\text{s}$ (75 m) x 1 Hz images from March 24. Each frame shows about 10° of rotation. See Fig. 3 caption.

FIG. 5. Sequence of $0.5 \mu\text{s}$ (75 m) x 1 Hz images from March 29. Each frame shows about 10° of rotation. See Fig. 3 caption.

FIG. 6. Comparison of echo spectra obtained at rotation phases 180° apart. Echo power spectral points in the March 24 spectrum are weighted sums extracted from the four echo-containing range rows in the 75 m x 1 Hz image (shown at the raw resolution on the left and smoothed on the right). Each spectrum covers about 10° of rotation.

FIG. 7. Constraints on the diameter, radar albedo, and visual geometric albedo of Bacchus. Radar albedo appears as a thick solid curve that is computed using Bacchus' radar cross section (Table VI). Thin solid curves denote 1-sigma uncertainty in the radar albedo that propagates from uncertainty in σ_{OC} . The distribution by taxonomic class of main-belt and near-Earth asteroid radar albedos is superimposed on the radar albedo curve and is plotted solely as a function of radar albedo. Allowed geometric albedos (dash-dot curve) were computed as a function of diameter from $\log p_v = 6.244 - 2\log D - 0.4H$ (Zellner 1979), where H is Bacchus' absolute magnitude (Table I). Mean and rms dispersions of the geometric albedos for the C, M, S, and E taxonomic classes (Tedesco 1989) are indicated by asterisks and adjacent thick curves. The geometric albedo of V-class asteroid 4 Vesta is shown with an asterisk (Tedesco 1989, Thomas *et al.* 1997). A vertical dashed line at $D_{\text{max}} = 0.6$ km denotes a lower bound on Bacchus' maximum pole-on

breadth, calculated from the maximum delay dispersion in 75 m x 1 Hz images obtained on March 24 and 29.

FIG. 8. Polar projection of Bacchus' ecliptic longitude and latitude on observation dates. Solar phase angles in degrees are in parentheses.

FIG. 9. Constraints on the density of Bacchus for a model consisting of two homogeneous spheres of equal density and radius in orbit about their mutual center of mass. Kepler's 3rd law and Bacchus' rotation period are used to compute the surface-to-surface separation of two lobes as a function of their diameter for densities between 0.5 and 3.0 g cm⁻³. The vertical dashed line indicates a lower bound on the lobe diameters from their 2-sigma delay extent in 75 m x 1 Hz images on March 29. This lower bound ignores radar shadowing and probably underestimates the actual diameters. The horizontal dashed line indicates an upper bound on the separation of the lobes under the assumption that dark pixels (with SNRs < 2) between the lobes in 75 m x 1 Hz images are devoid of mass. The shaded region indicates allowed densities. This figure shows that if Bacchus' lobes were not in contact, then, by this model, the lobes' bulk density would have to be less than 0.5 g cm⁻³.

FIG. 10. Renderings of (a) one-lobe and (b) two-lobe Bacchus shape models. Each model is shown at 10° rotation phases that correspond to delay-Doppler images (Figs. 4 and 5) obtained on March 24 and 29. For each average rotation phase, the top row shows a plane-of-sky projection of the shape model, the second row shows modeled delay-Doppler images, the third row shows observed delay-Doppler images, and the bottom row shows residuals. Doppler frequency

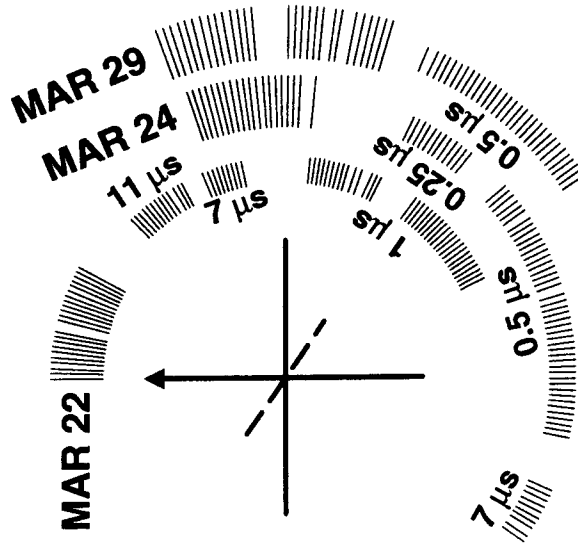
increases from left to right and time delay increases from top to bottom. The shape renderings use Lambertian scattering and appear at a phase angle of 0° .

FIG. 11. Sequence of plane-of-sky projections of single lobe (a) and two lobe (b) shape models, cw spectra, modeled cw spectra, and residuals shown at $\sim 10^\circ$ rotation phase intervals for each day.

FIG. 12. Lightcurve data (circles) and modeled lightcurves for the single-lobe and two-lobe models. The lightcurves are shown as a function of UTC on each night and are expressed in absolute magnitudes (R-filter).

FIG. 13. Normal reflection coefficient R for principal meteorite types (reproduced from Ostro *et al.* 1991a). The curves on the right show R as a function of porosity based on the average of three empirically-determined functions (Ostro *et al.* 1985; Garvin *et al.* 1985; Ulaby *et al.* 1990) over the range of typical lunar soil porosities. These curves are probably accurate to within $\sim 25\%$. Ovals show ranges of R expected for meteorite types based on laboratory investigations of “loaded dielectrics” (Kelly *et al.* 1953; Nielson 1974; Pettengill *et al.* 1988). Cross-hatched regions denote measurements of R for six individual meteorites (Campbell and Ulrichs 1969).

$P = 14.90$ hours



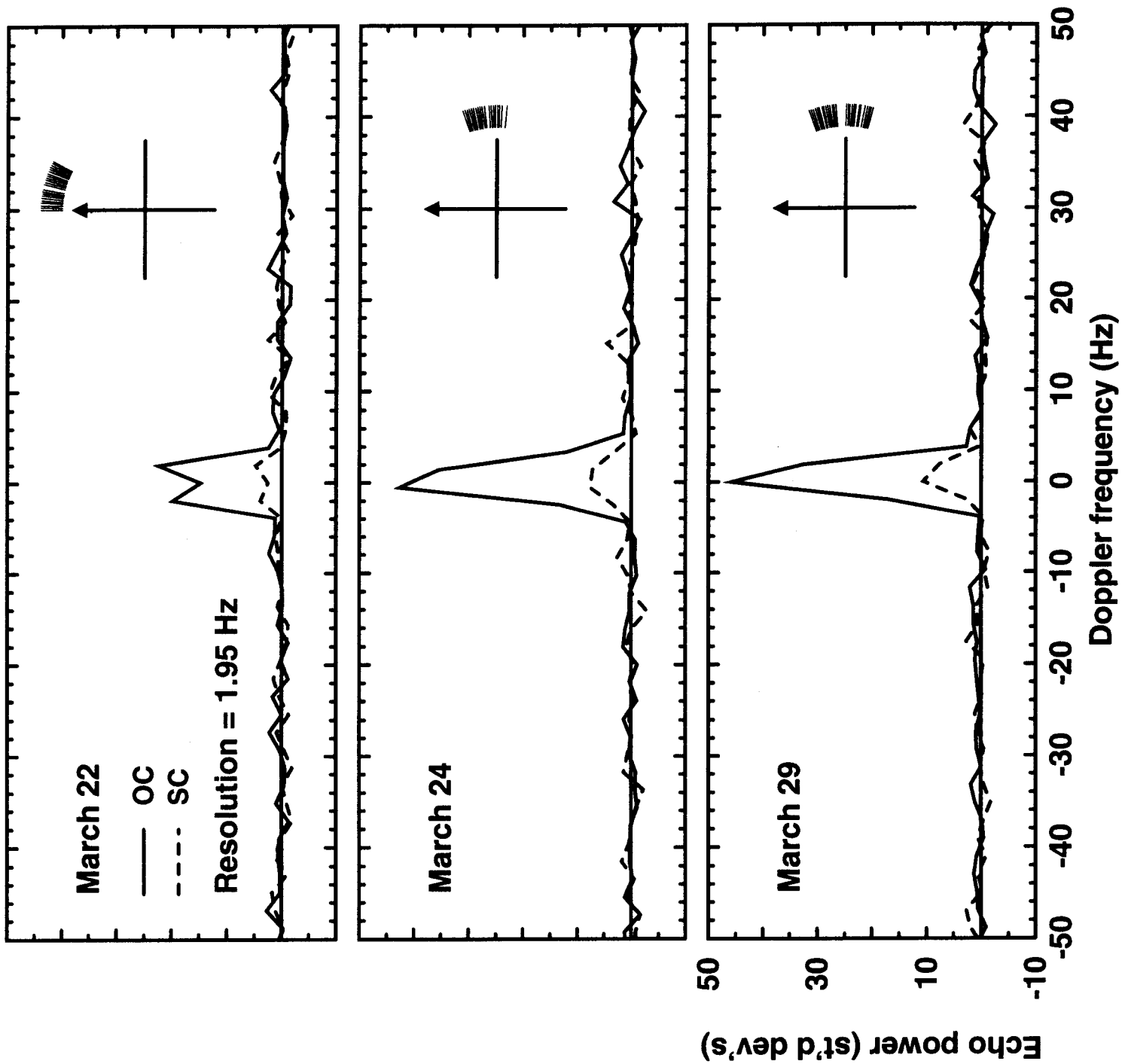
Ranging setups

- 11 μ s (1650 m) x 5.6 Hz
- 7 μ s (1050 m) x 5.9 Hz
- 1 μ s (150 m) x 1.0 Hz
- 0.5 μ s (75 m) x 1.0 Hz
- 0.25 μ s (37.5 m) x 0.5 Hz

Long segments = cw (1.95 Hz)

Short segments = ranging

Zero-phase epoch: 1996 March 22 17:37:31 UTC



MARCH 22

150 m x 1 Hz

Breadth (m/cos δ)

-900 0 900

Range (m)

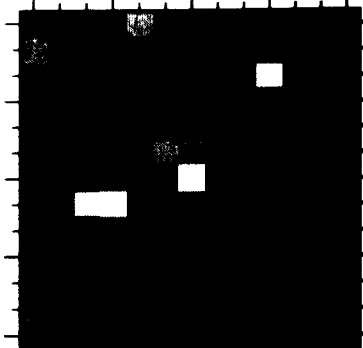
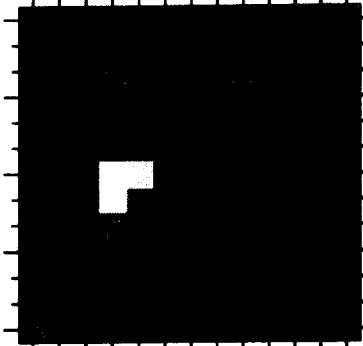
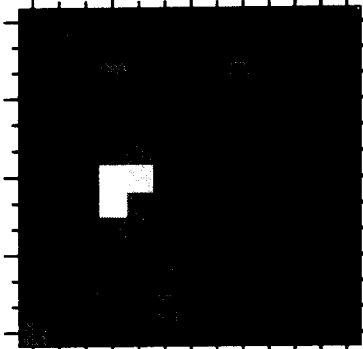
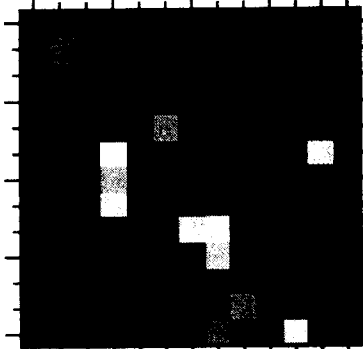
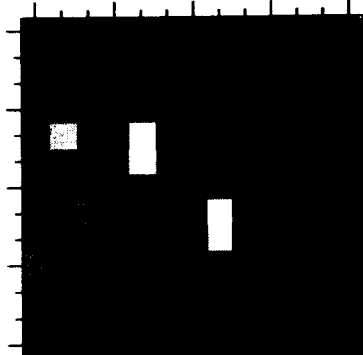
-900

-450

0

450

900



-5 0 5

Doppler frequency (Hz)



Echo power (st'd dev's)



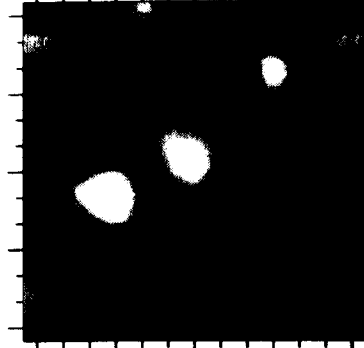
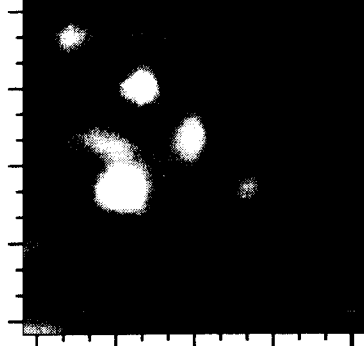
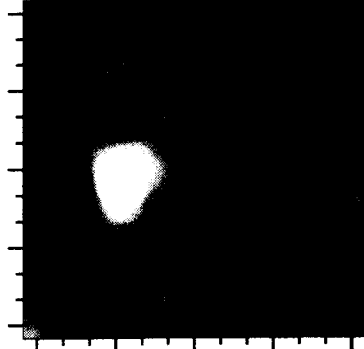
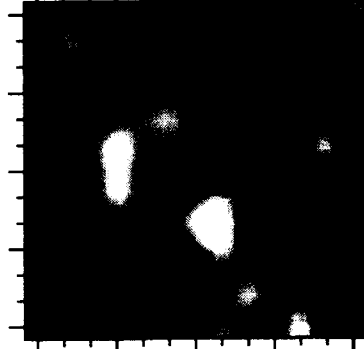
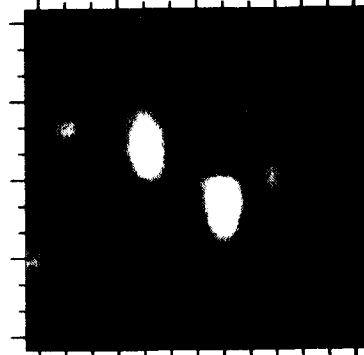
21:47:16 (100°)

22:12:54 (111°)

23:01:25 (130°)

23:24:15 (139°)

23:48:15 (150°)



MARCH 24

75 m x 1 Hz

Breadth (m/cos δ)

-900 0 900

Range (m)

-900

-450

0

450

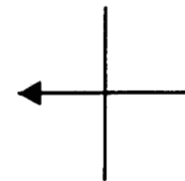
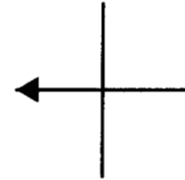
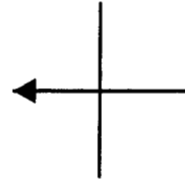
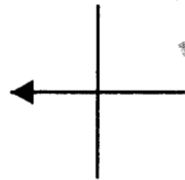
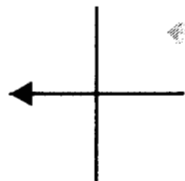
900

Doppler frequency (Hz)

-5

0

5



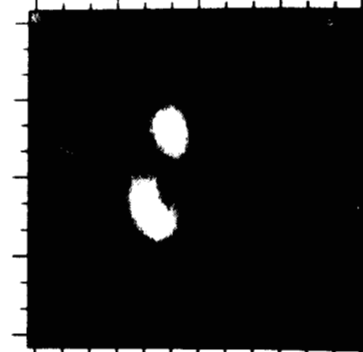
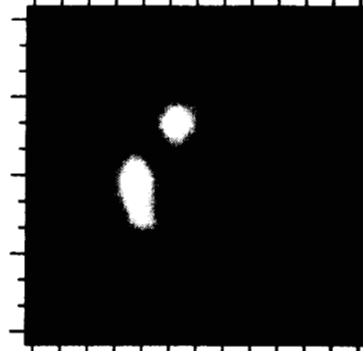
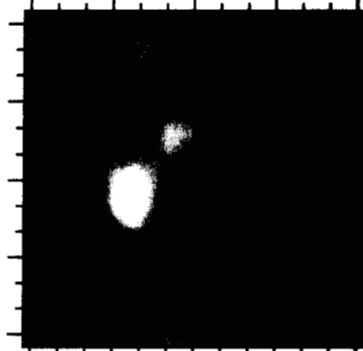
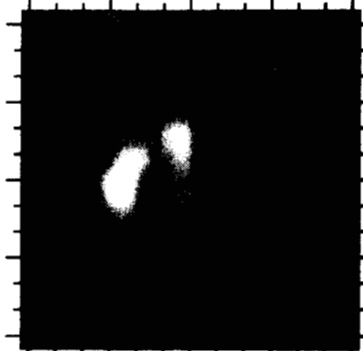
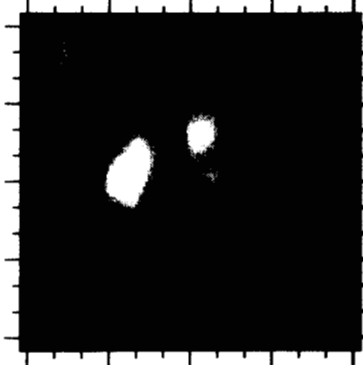
20:17:34 (144°)

20:45:28 (155°)

21:14:56 (167°)

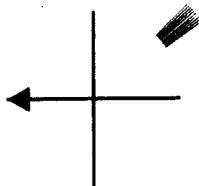
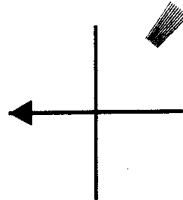
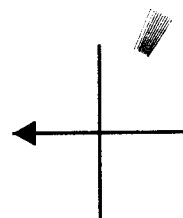
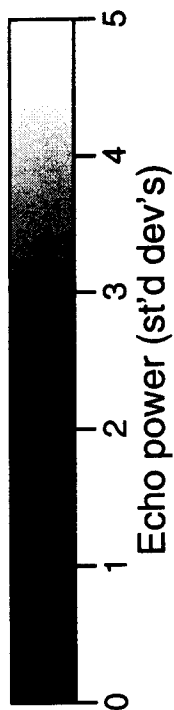
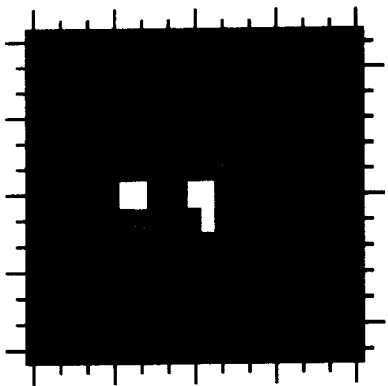
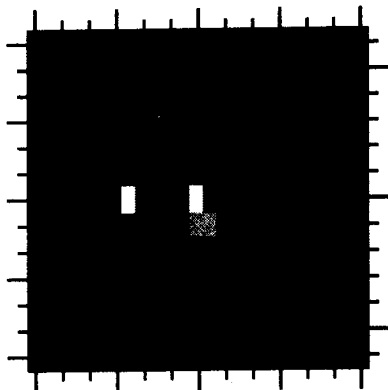
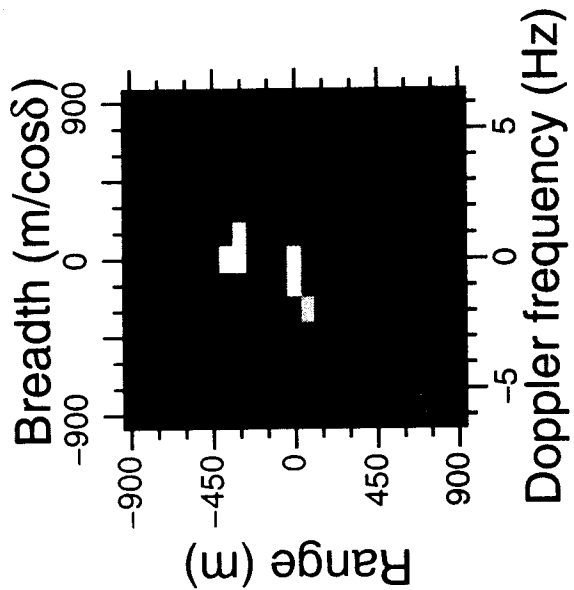
21:41:18 (178°)

22:06:31 (188°)

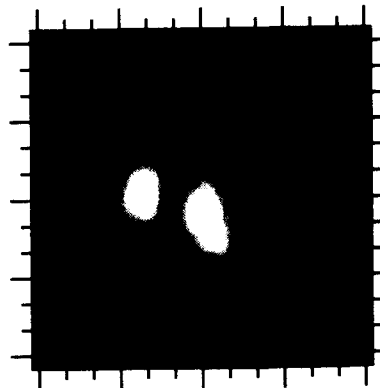


MARCH 29

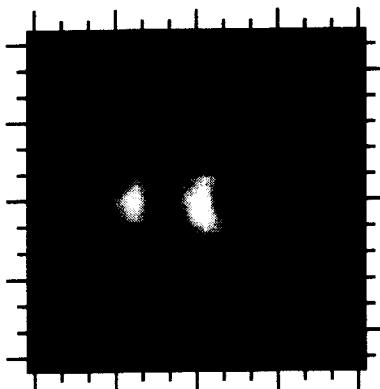
75 m x 1 Hz



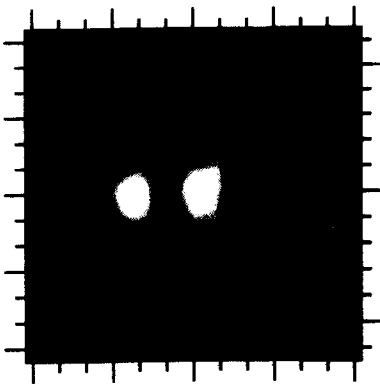
18:26:20 (119°)



18:53:56 (130°)



19:21:55 (141°)



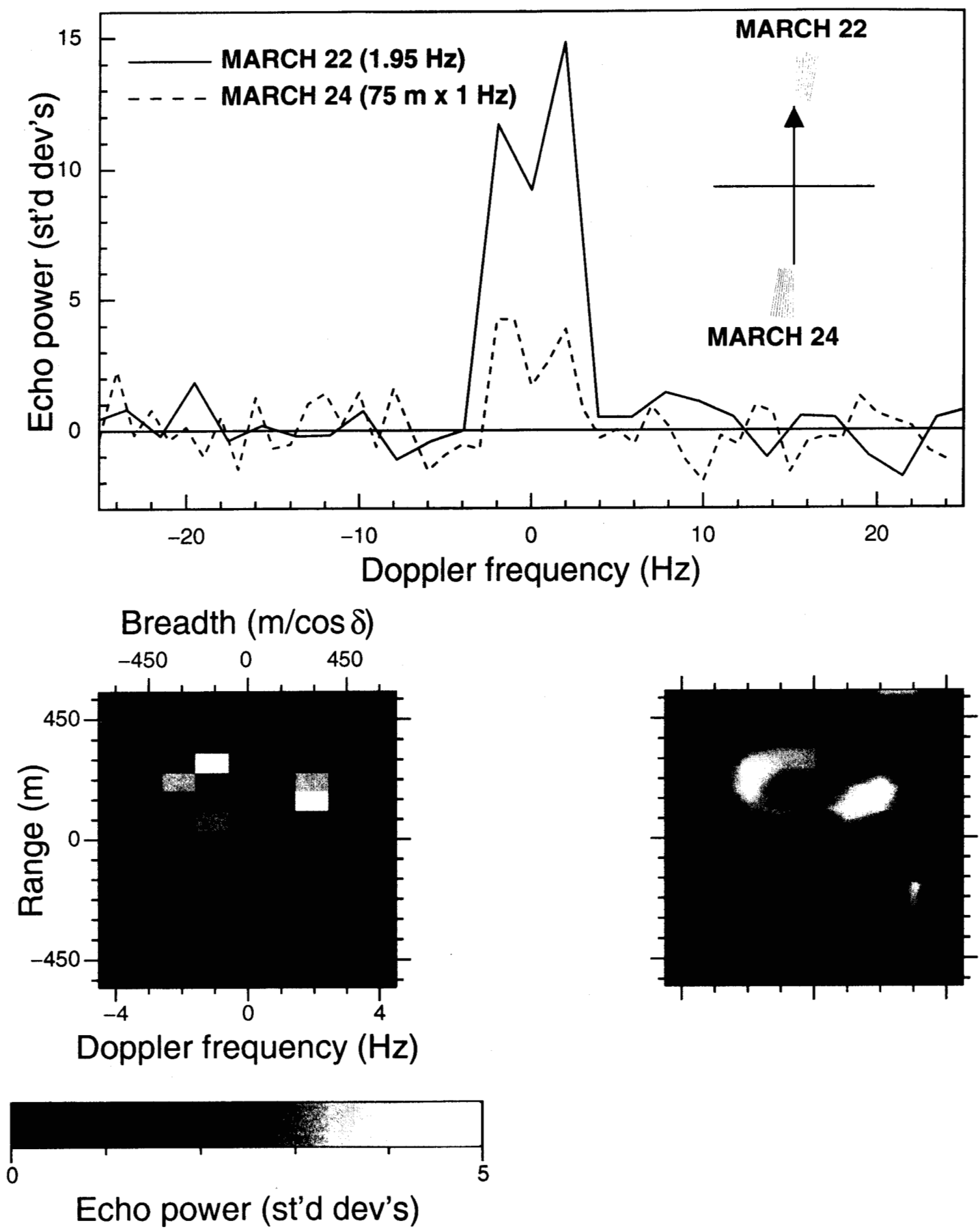
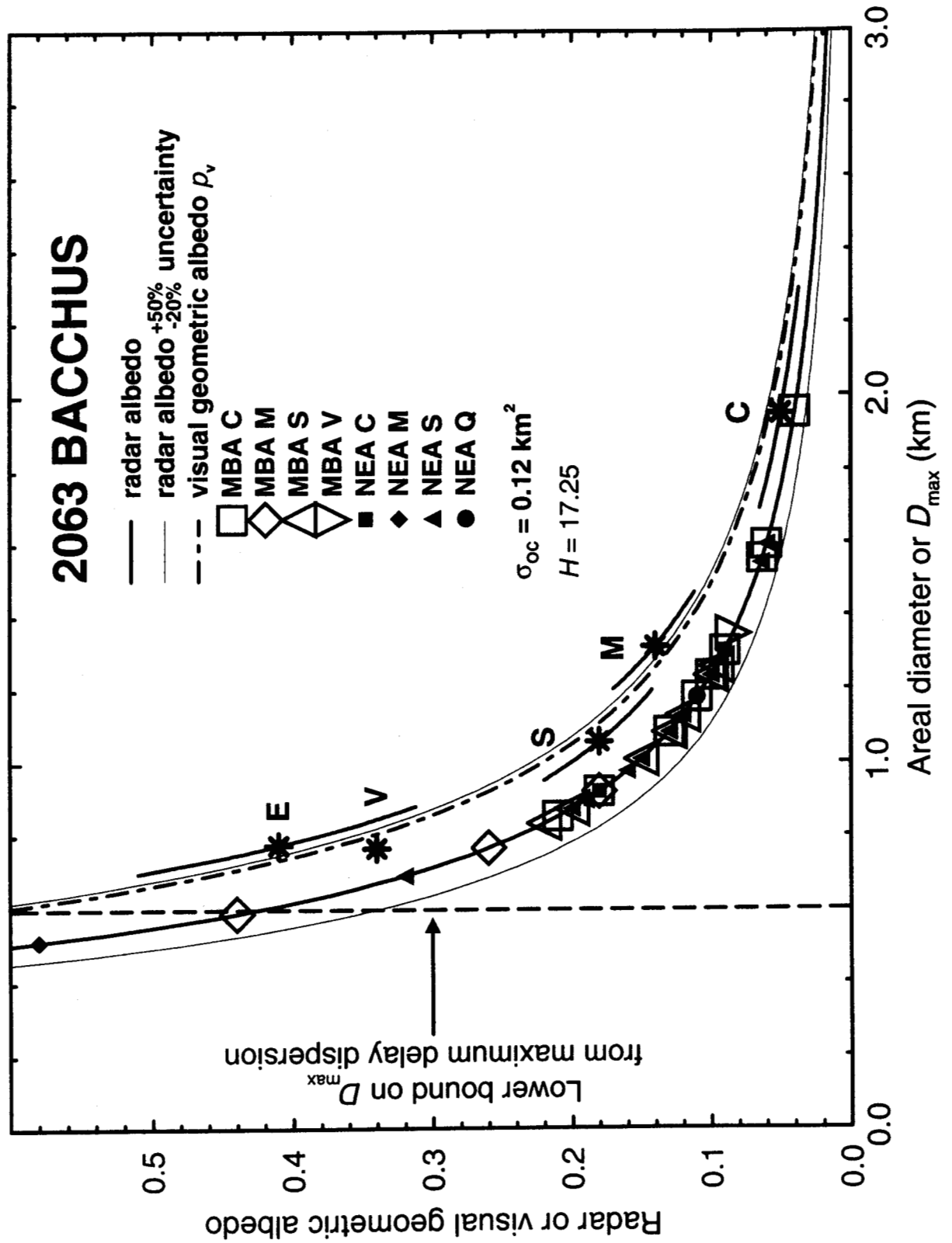
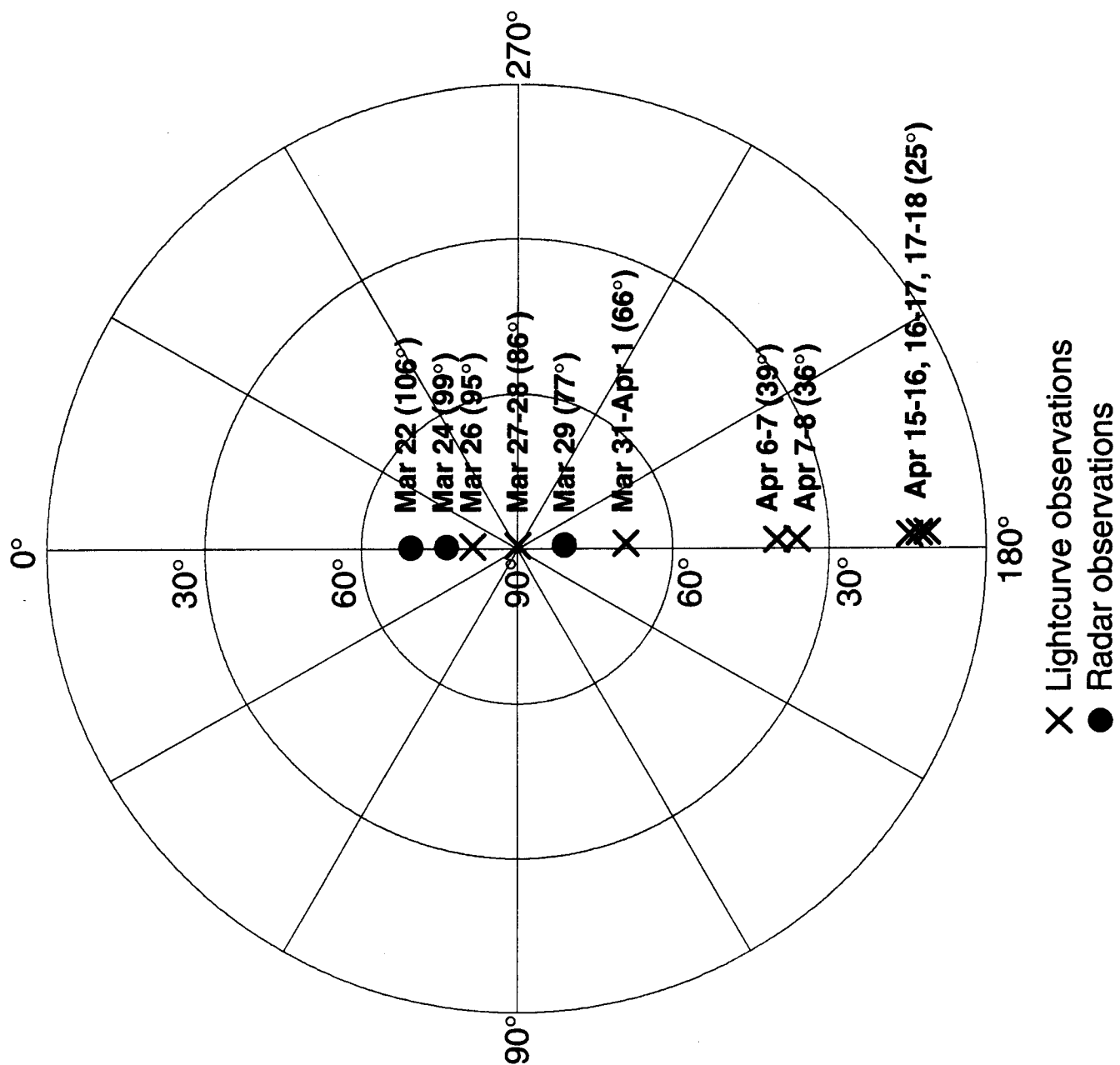
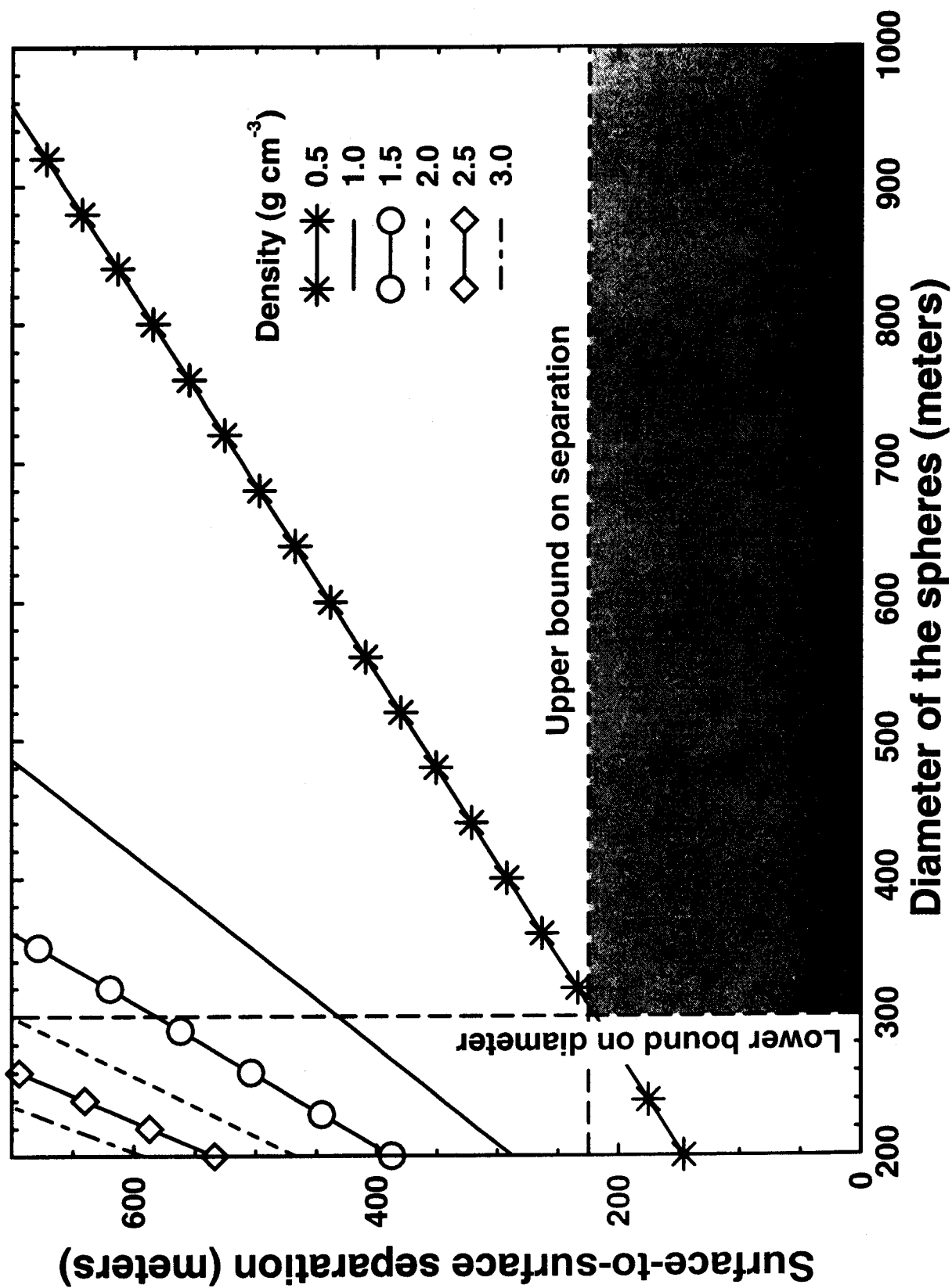


Fig. 6

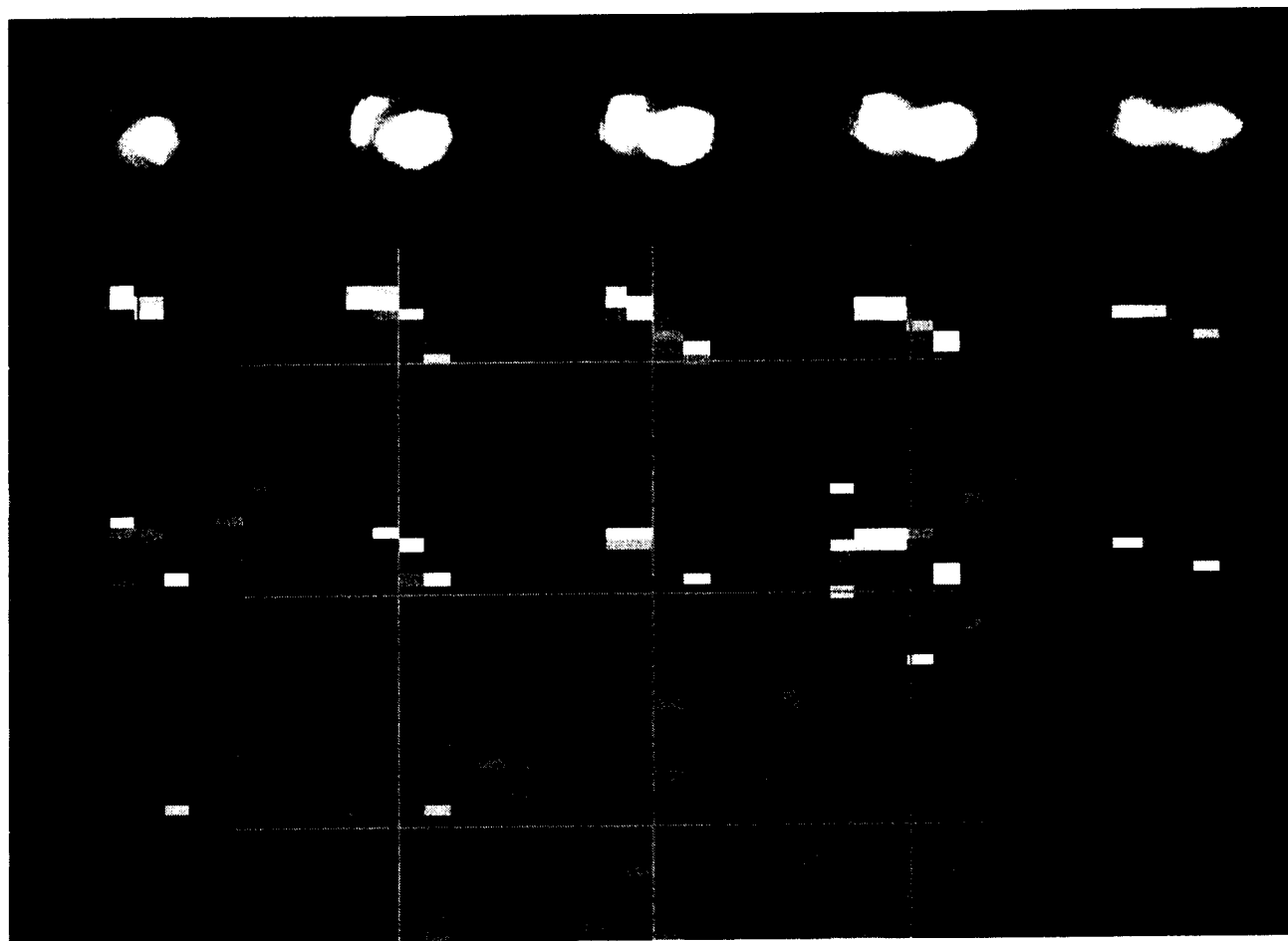




X Lightcurve observations
● Radar observations



MARCH 24



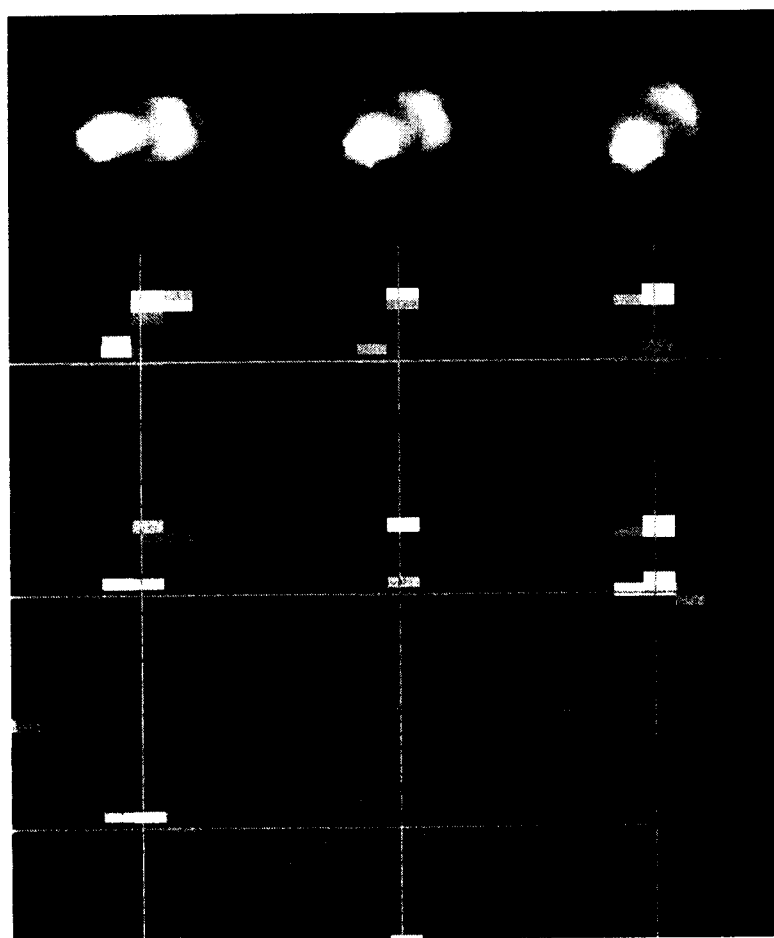
**SHAPE
MODEL**

**MODELED
IMAGES**

DATA

RESIDUALS

MARCH 29



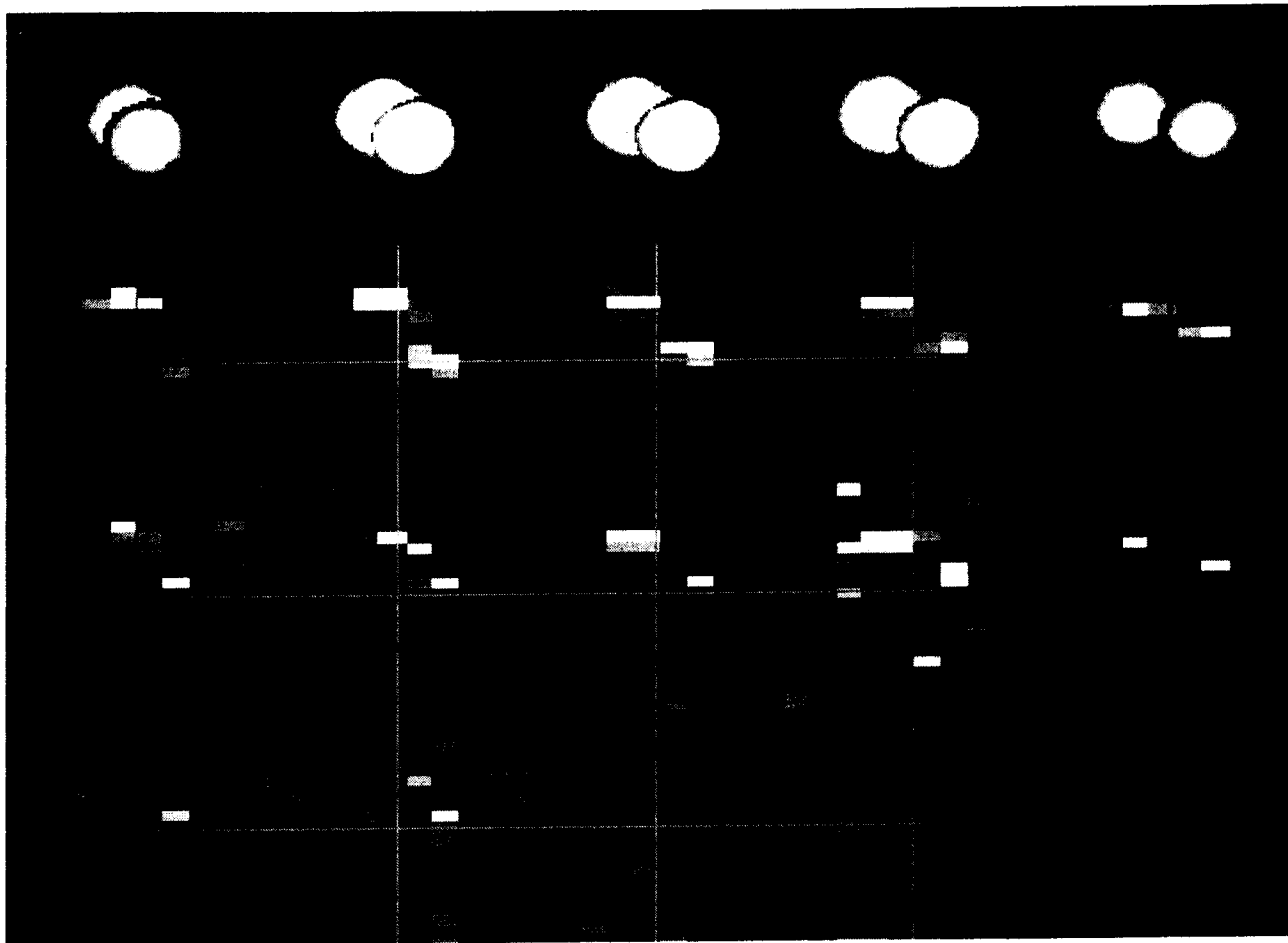
**SHAPE
MODEL**

**MODELED
IMAGES**

DATA

RESIDUALS

MARCH 24



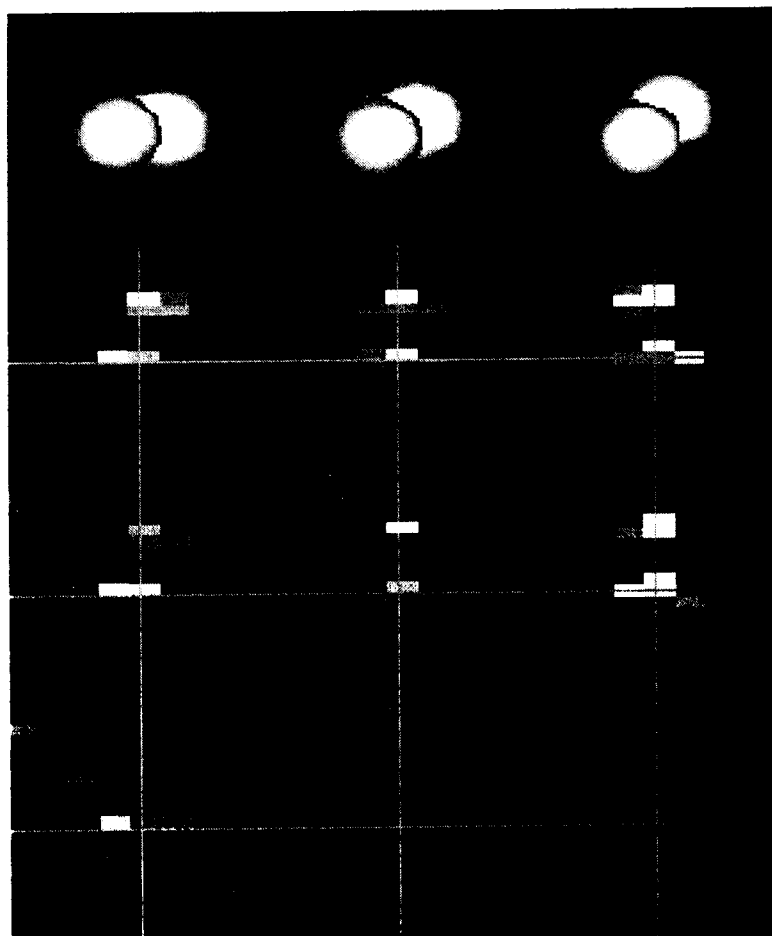
**SHAPE
MODEL**

**MODELED
IMAGES**

DATA

RESIDUALS

MARCH 29



**SHAPE
MODEL**

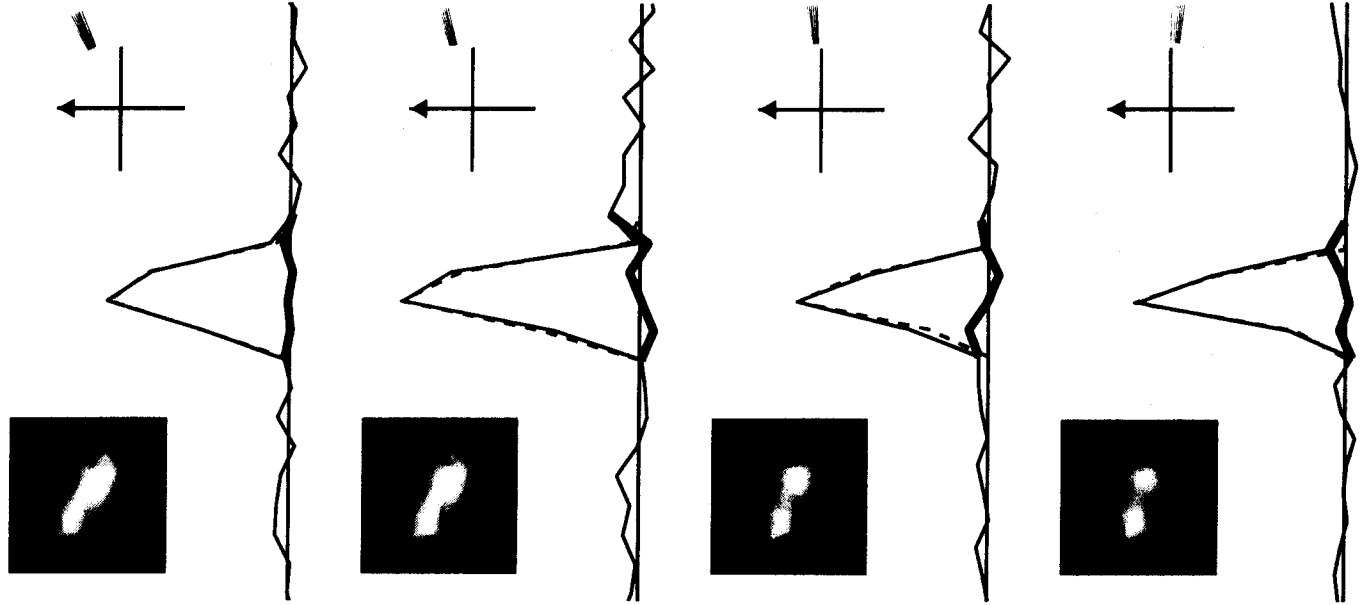
**MODELED
IMAGES**

DATA

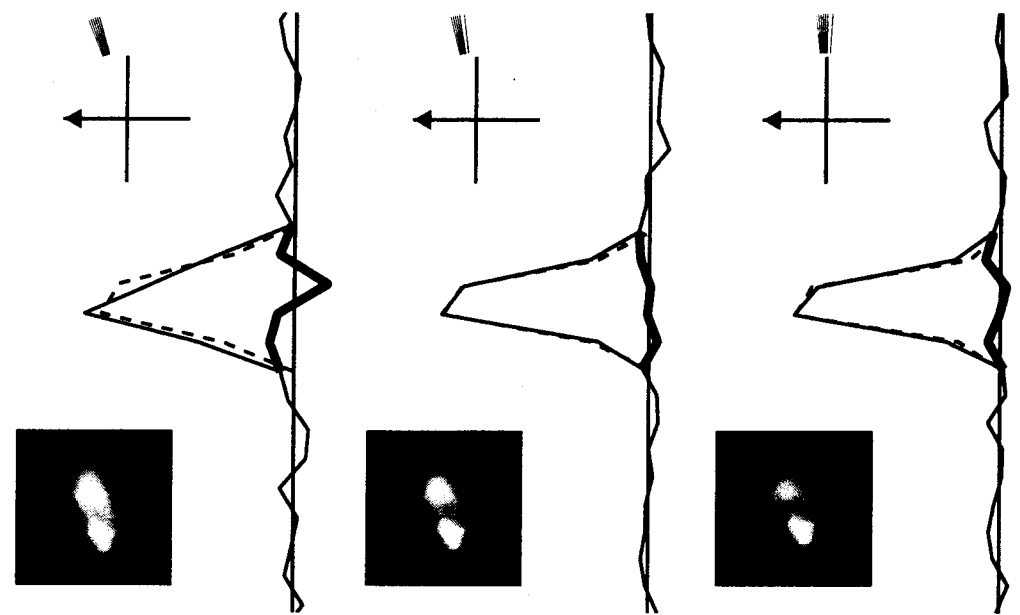
RESIDUALS

SINGLE LOBE MODEL

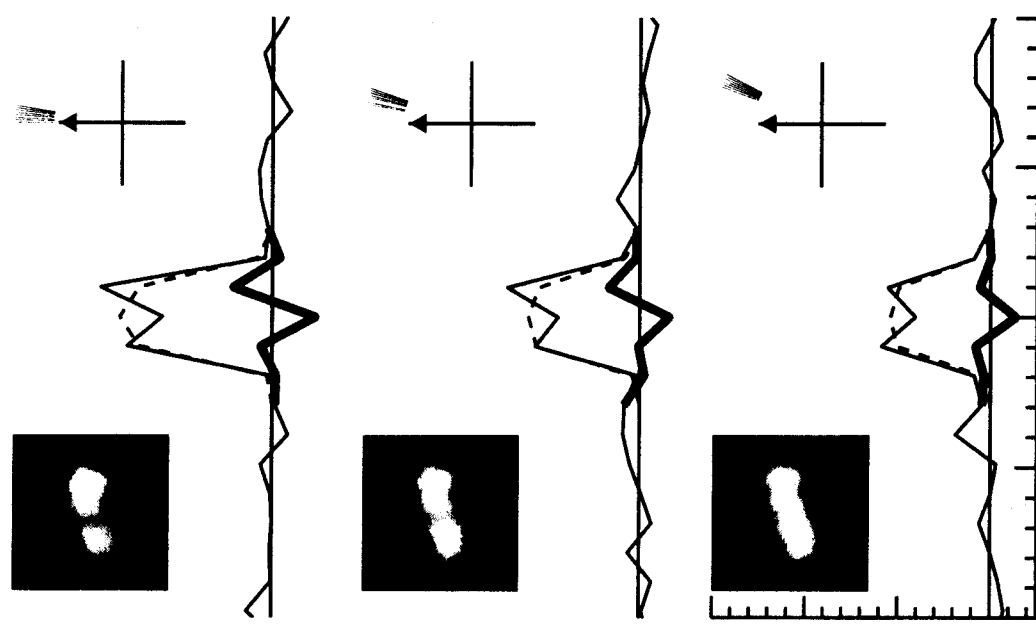
MARCH 29



MARCH 24



MARCH 22



- Data
- - - Modeled Spectra
- Residuals

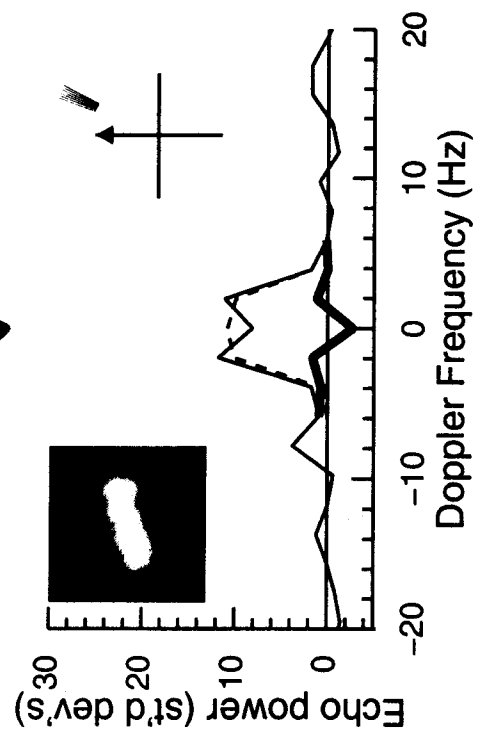
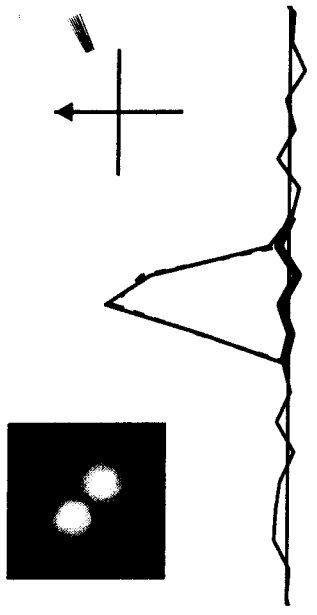


FIG. 11 A

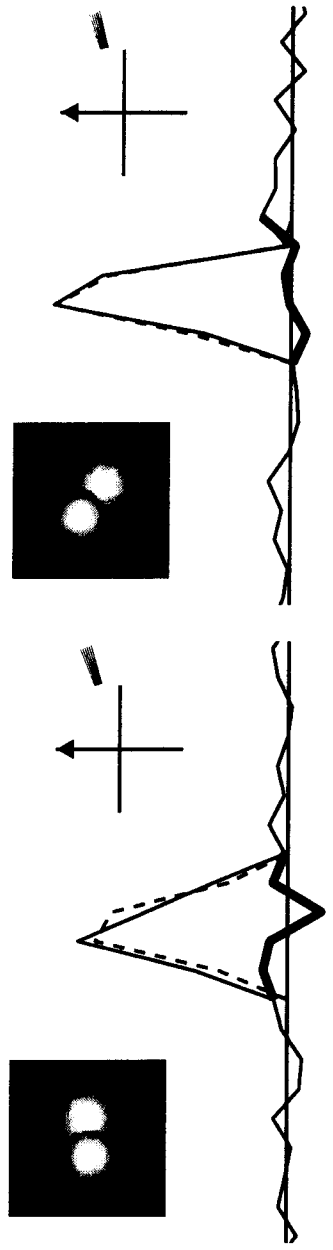
TWO LOBE MODEL

- Data
- - - Modeled Spectra
- Residuals

MARCH 29



MARCH 24



MARCH 22

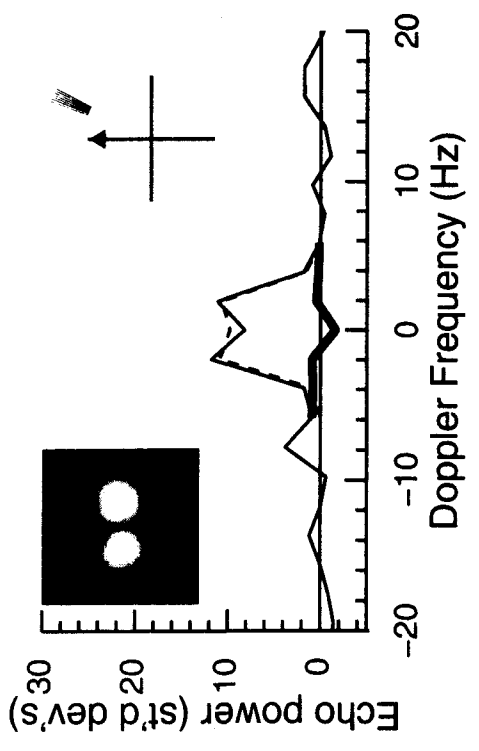
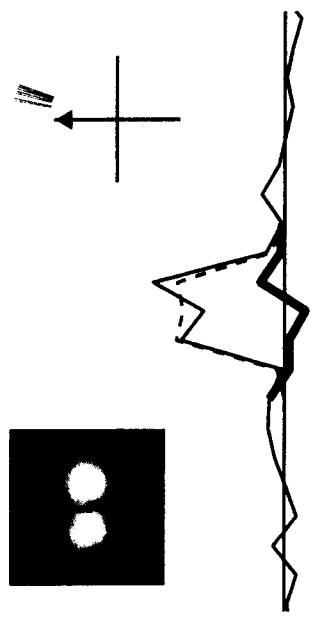
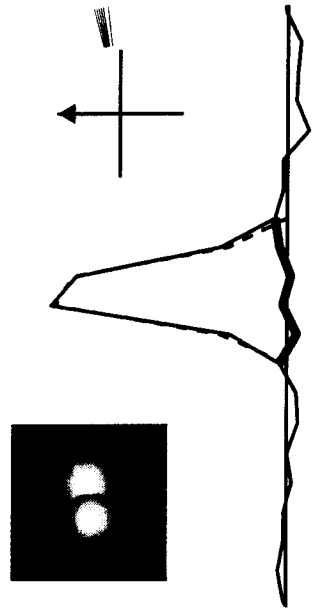
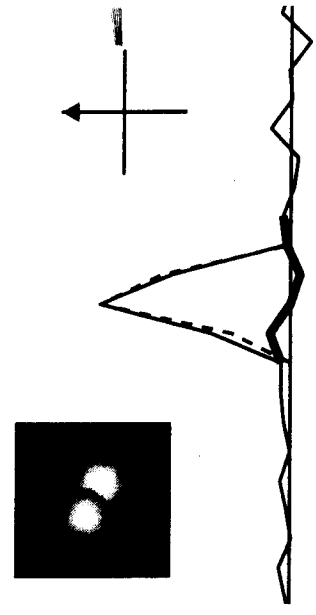
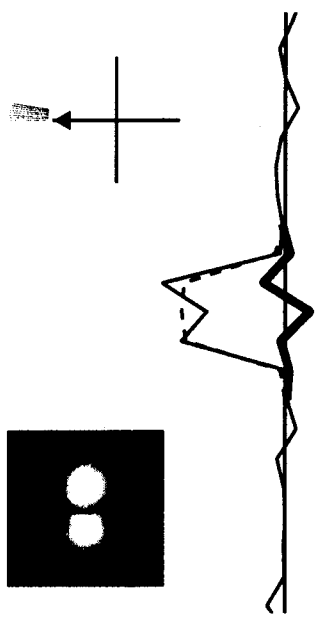


FIG. 1113

Single Lobe Model

Two Lobe Model

